

IMU Error Modeling Tutorial

INS state estimation with real-time sensor calibration

Jay A. Farrell, Felipe O. Silva, Farzana Rahman, J. Wendel

POC: J. Farrell (farrell@ece.ucr.edu)

October 15, 2021

Autonomous vehicle technology is rapidly advancing. Key enabling factors are the advancing capabilities and declining cost of computing and sensing systems that enable sensor fusion for awareness of the vehicle's state and surroundings. For control purposes, the vehicle state must be estimated accurately, reliably, at a sufficiently high sample rate, and with a sufficiently high bandwidth. For systems with high bandwidth, these requirements are often achieved by an aided inertial navigation system (INS) [1], [2], [3], [4], [5], [6]. An INS integrates data from an inertial measurement unit (IMU) through a kinematic model at the high sampling rate of the IMU to compute the state estimate. An aided INS corrects this state estimate using data from aiding sensors (e.g., vision, LIDAR, RADAR, Global Navigation Satellite System (GNSS)). State estimation by sensor fusion may be accomplished by any of a variety of methods: Kalman filter (KF) [7], [8], [9], [10], [11], extended Kalman filter (EKF) [12], [13], [14], [15], unscented Kalman filter (UKF) [16], [17], [18], particle filter (PF) [19], [20], [21], maximum a posteriori (MAP) optimization [22], [23], [24], [25], [26], [27].

A data fusion system that combines the IMU and aiding sensor data will be able to achieve improved performance by real-time calibration if it incorporates an IMU error model in state-space form. The IMU manufacturer supplies a data sheet characterizing the expected IMU performance. In accordance with the specification standards [28], [29], [30], this performance is typically stated in terms of the Allan Variance (AV). However, it is not immediately clear how to translate the AV information from such data sheets into a suitable state-space model. Such translation methods have been known and used for several decades [31], [32], [33], [34], [35], [36], [37], [38], [39], [40]. Despite their importance, a clear tutorial exposition of the underlying ideas, issues, and trade-offs is not available in the existing literature. Providing such a tutorial discussion is the purpose of this article. The long history of these ideas and issues relative to successful applications is discussed in the sidebar "Aided INS History".

I. APPLICATION CONTEXT

The INS design is based on a vehicle kinematic model of the form,

$$\dot{\vec{x}}_v(t) = f(\vec{x}_v(t), \vec{u}(t)), \quad (1)$$

where \vec{x}_v represents the state of the vehicle and $\vec{u} \in \mathbb{R}^6$ represents the system inputs (i.e., specific force and angular rate vectors). A typical vehicle state vector might include subvectors for position, velocity, and attitude. The navigation system numerically solves

eqn. (1) based on a measurement of the signal $\vec{u}(t)$,

$$\hat{\vec{x}}_v(t) = f(\hat{\vec{x}}_v(t), \hat{\vec{u}}(t)), \quad (2)$$

where $\hat{\vec{u}}(t)$ is computed from the IMU measurement $\tilde{\vec{u}}(t)$ using calibration factors that are estimated in real-time. A simplified two-dimensional inertial navigation example illustrating these ideas is presented in the sidebar "Simplified INS Example".

For a scalar signal, the model relating the sensor measurement $\tilde{u}(t)$ to the desired signal $u(t)$ has the form (see Annex B in [28], [29])

$$\tilde{u}(t) = u(t) + d(\tilde{u}(t)) + z(t). \quad (3)$$

The measurement $\tilde{u}(t)$ of the desired signal $u(t)$ is corrupted by *deterministic errors* $d(\tilde{u}(t))$ and cumulative *stochastic error* $z(t)$. Deterministic errors are the sensor imperfections that are sufficiently well behaved to be modeled with an analytical model, with unknown deterministic coefficients. Some of these coefficients exhibit only minor variations during the lifetime of the instrument. These can be estimated and compensated in a factory calibration process. Other deterministic errors like turn-on biases can be estimated in real-time via state augmentation. Forms of deterministic errors might include scale factor error, nonlinearity, g -sensitivity for gyros, or non-orthogonality and axes cross-coupling for vector measurements $\vec{u}(t)$ [5], [41], [42]. See the "Deterministic Errors" subsection in the "Discussion of Issues and Tradeoffs". The focus of this article is the stochastic error denoted by $z(t)$, which may arise from a variety of physical phenomena (see the "Background" section). The stochastic errors are distinct each time that the instrument is turned on, vary as a function of time, and cannot be predicted based on the sensor measurement $\tilde{u}(t)$.

For clarity and simplicity of the tutorial presentation, the majority of this tutorial will treat $z(t)$ as a scalar signal. The underlying ideas apply to each of the three accelerometers and three gyros in a six degree-of-freedom IMU for the development of the full IMU stochastic error model.

A. State Estimation Error Model

While the navigation system propagates the vehicle state vector through time by integrating the nonlinear model of eqn. (2), error denoted by $\delta\vec{x}_v(t) = \vec{x}_v(t) - \hat{\vec{x}}_v(t)$ will develop between the actual and estimated state vectors. Regardless of the choice of representation of the vehicle attitude (e.g., direction cosine matrix or quaternion) the attitude error can be represented by a vector with three components. Therefore, the vehicle error state contains

subvectors for position, velocity, and attitude error, each being a vector with three components such that $\delta \vec{x}_v(t) \in \mathbb{R}^{n_v}$ with $n_v = 9$. This vehicle state error vector can be estimated in real-time using measurements from the aiding sensors, e.g. [10], [13], [12], [31], [43], [44]. The estimation algorithm incorporates a linearized state-space model for the error state, which has the form,

$$\delta \dot{\vec{x}}_v(t) = F(t) \delta \vec{x}_v(t) + G(t) \delta \vec{u}(t), \quad (4)$$

where $F(t) = \left. \frac{\partial f(\vec{x}, \vec{u})}{\partial \vec{x}} \right|_{\hat{\vec{x}}(t), \hat{\vec{u}}(t)}$, $G(t) = \left. \frac{\partial f(\vec{x}, \vec{u})}{\partial \vec{u}} \right|_{\hat{\vec{x}}(t), \hat{\vec{u}}(t)}$, and $\delta \vec{u}(t) = \vec{u}(t) - \hat{\vec{u}}(t)$. See the example $F(t)$ and $G(t)$ matrices in the “Simplified INS Example” sidebar. This state-space error model is not complete until the IMU error model for $\delta \vec{u}(t)$ is specified. For state estimation, it is required that the IMU error model be in state-space form.

The real-time state estimation process is designed to estimate the augmented state vector

$$\vec{z}(t) = \begin{bmatrix} \delta \vec{x}_v(t)^\top & \vec{x}_d(t)^\top & \vec{x}_z(t)^\top \end{bmatrix}^\top \in \mathbb{R}^{n_x} \quad (5)$$

comprised of the vehicle error state vector $\delta \vec{x}_v(t) \in \mathbb{R}^{n_v}$, the vector $\vec{x}_d(t) \in \mathbb{R}^{n_d}$ augmented to enable calibration of the IMU deterministic errors, and the vector $\vec{x}_z(t) \in \mathbb{R}^{n_z}$ augmented to enable calibration of the IMU stochastic errors. The total number of error states $n_x = n_v + n_d + n_z$, where n_v is the number of vehicle error states, n_d is the number of states augmented to calibrate deterministic errors, and n_z is the number of states augmented to calibrate stochastic errors. The process of state augmentation as it relates to the problems of interest is discussed in the “State Augmentation” sidebar. The presentation herein will focus entirely on the stochastic IMU errors whose cumulative effect in eqn. (3) is denoted by $\vec{z}(t)$. The majority of this article will focus on a single IMU output for which a scalar $z(t)$ is sufficient. The “Discussion of Issues and Trade-offs” section considers the vector $\vec{z}(t)$ case.

Denote the state-space model for scalar $z(t)$ as,

$$\dot{\vec{x}}_z(t) = A_z \vec{x}_z(t) + B_z \vec{\omega}_z(t), \quad (6)$$

$$z(t) = C_z \vec{x}_z(t) + \eta_z(t) \quad (7)$$

where $A_z \in \mathbb{R}^{n_z \times n_z}$, $B_z \in \mathbb{R}^{n_z \times p}$ and $C_z \in \mathbb{R}^{1 \times n_z}$. The parameter p represents the number of distinct and independent noise processes in the differential equation portion of the IMU error model. The parameter n_z represents the number of states in the IMU stochastic error model. The random signals $\vec{\omega}_z(t)$ and $\eta_z(t)$ are mutually independent Gaussian white noise processes with Power Spectral Densities (PSD) $S_{\omega_z} \in \mathbb{R}^{p \times p}$ and $S_{\eta_z} \in \mathbb{R}$, respectively. The elements of $\vec{\omega}_z(t)$ are assumed to be independent which yields S_{ω_z} being diagonal.

The designer must be judicious in the choice of the model structure, particularly n_z and p , as the overall model will have $6n_z$ states and $6p$ independent noise sources.

B. Power Spectral Density for Linear State-Space Systems

Corresponding to the state-space model in eqns. (6-7), the frequency domain model is

$$Z(s) = T(s) \Omega_z(s) + \eta_z(s) \quad (8)$$

where s is the Laplace variable and the transfer function model from $\omega_z(t)$ to $z(t)$ has the form,

$$T(s) = C_z (sI - A_z)^{-1} B_z$$

which has one row and p columns. The symbols $Z(s)$, $\Omega_z(s)$, and $\eta_z(s)$ represent the Laplace transforms of the signals $z(t)$, $\omega_z(t)$, and $\eta_z(t)$. Therefore, the power spectral density corresponding to signal $z(t)$ is,

$$S_z(\omega) = T(j\omega) S_{\omega_z} T(-j\omega)^T + S_{\eta_z}. \quad (9)$$

Assuming that all elements of the driving noise vector $\omega_z(t)$ and the output noise $\eta_z(t)$ are mutually independent and white, this simplifies to,

$$S_z(\omega) = \sum_{i=1}^p T_i(j\omega) T_i(-j\omega) S_{\omega_{z_i}} + S_{\eta_z}, \quad (10)$$

with,

$$T_i(s) = C_z (sI - A_z)^{-1} B_{z_i} \quad (11)$$

where $T_i(s)$ is the (scalar) transfer function from the i -th component of $\vec{\omega}_z(t)$ to $z(t)$, and $B_{z_i} \in \mathbb{R}^{n_z \times 1}$ is the i -th column of B_z . Each $T_i(s)$ is the ratio of a numerator and denominator polynomial in s and S_{z_i} is a positive real number. Therefore, each $T_i(j\omega)T_i(-j\omega)$ (and $S_z(\omega)$) will always be the ratio of polynomial functions of only the even powers of the Laplace variable s . Examples demonstrating this fact are presented in the sidebar entitled “Finite Dimensional Linear State-Space Systems have Even Power Spectra”.

The fact stated in the last sentence leads to one of the main challenges in the IMU error modeling approach, because some of the IMU stochastic error components have PSDs that cannot be exactly fit by the terms in the summation of eqn. (10). Therefore, the designer must make judicious choices in the approximate state-space model to achieve satisfactory trade offs. This will be further discussed in the section entitled “Modeling via Independent Noise Sources”.

C. Available Error Specification Information

To characterize the quality of an IMU, per the IEEE specifications [28], [29], [30], the manufacturer provides the Allan Variance (AV) plot, Allan Standard Deviation (ASD) plot, or parameters extracted from them. An ASD graph can both help instrument designers understand and improve their sensors, and

TABLE I
DOMINANT ERRORS IN CONSUMER GRADE IMUS

Noise type (Coef.)	Coef. unit	Allan Variance Acc: (m/s ²) ² Gyro: (deg/s) ²	PSD Acc: m ² /s ³ Gyro: deg ² /s
Ang./Vel. random walk, N	Acc: m/s ^{3/2} Gyro: deg/s ^{1/2}	$\frac{N^2}{\tau}$	N^2
Bias instability, B	Acc: m/s ² Gyro: deg/s	$\frac{2 B^2 \ln(2)}{\pi}$	$\frac{B^2}{2 \pi f}$
Rate/Accel. random walk, K	Acc: m/s ^{5/2} Gyro: deg/s ^{3/2}	$\frac{K^2 \tau}{3}$	$\left(\frac{K}{2 \pi f} \right)^2$

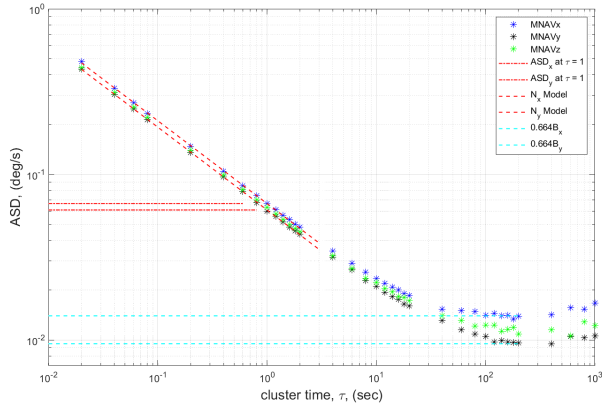


Fig. 1. ASD plots for three Crossbow μ Nav gyros [36], [45], with straight line approximations for dominant errors. Sampling interval is $T = 0.02$ s.

communicate expected performance to perspective users. Within the context of this article, the main topic is how an INS designer can use information from an ASD plot to specify the parameters of the state-space model in eqns. (6-7).

Example ASD plots are shown in Figs. 1 and 2. Fig. 1 displays the ASD plots for three gyros in a Crossbow μ Nav IMU [45]. These ASD are computed from data provided by the authors of [36]. The blue, black, and green asterisks (“*”) mark the ASD data points. The ASD plot in Fig. 2 is computed from manufacturer supplied data obtained from an IMU mounted on a large marble slab on top of a vibration isolation system. The blue x’s in Fig. 2 mark the ASD data points. The horizontal axis of each ASD plot is the cluster time (or size), with the symbol τ , measured in seconds. Note that the ASD plots in these two figures have both similarities and differences. Both decrease with the characteristic slope of $-1/2$ for small cluster sizes, as indicated by the red dashed tangent line in each figure. Then, both level off to a slope of zero, at values indicated by the dashed cyan tangent lines. Finally, for larger cluster sizes, the ASD in Fig. 2 increases with a slope of $1/2$, as indicated by the tangent line drawn with black dashes. For cluster times as large as $\tau = 1000$ seconds, the ASD plots in Fig. 1 do not (strongly) exhibit this increase with slope $1/2$. The value of τ and the ASD value at which these changes occur is distinct for each instrument. They specify certain parameters that are useful both for comparing the performance of inertial instruments and for evaluating trade-offs in the construction of the IMU stochastic error model.

D. Summary

This tutorial presents an example method, and discusses issues and trade offs, related to the navigation system design: (1) using the AV information to specify the continuous-time parameters (e.g., p , n_z , A_z , B_z , C_z , S_z , and S_η) for an IMU state-space stochastic error model; (2) transforming this continuous-time model to the discrete-time state-space error model parameters (Φ , Q_{z_d} , H , Q_{η_d}) that are required for implementation of the state estimator; and, (3) verifying the IMU model relative to the AV information. Some previous articles have addressed some of the aforementioned topics [32], [34], [36], [39], [43], [44], [46],

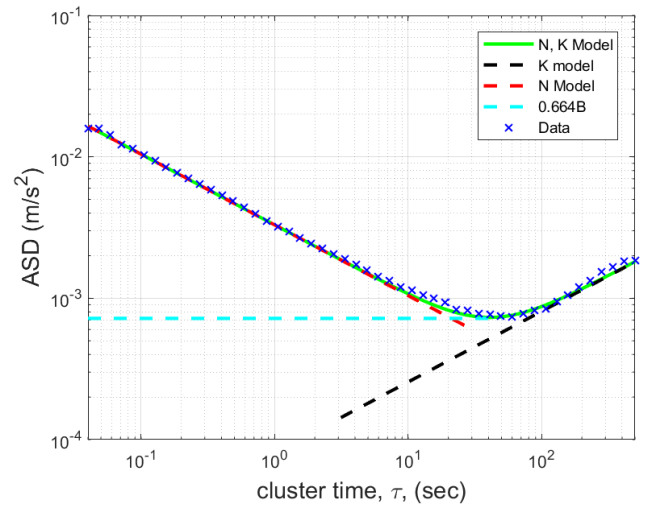


Fig. 2. Accelerometer ASD plot for the NV IMU-1000 from Nav Technology, with straight line approximations for dominant errors. Sampling interval is $T = 0.01$ s.

[47]. The goal of this article is to clearly and comprehensively present the background and main ideas in a tutorial fashion, using notation and terminology consistent with instrument specification standards [28], [29]. Examples are included throughout to clarify issues.

II. PROBLEM STATEMENT

The purpose of this article is to discuss methods, issues, and trade-offs related to developing a model that quantitatively communicates to the state estimation algorithm the nature of the stochastic portion of the IMU error. The inputs to this error model will be random signals.

The available information from the manufacturer for the model development is the AV or ASD characterization. The actual IMU output data from the experiments that produce these characterizations are not available to the designer; therefore, system identification methods are not applicable.

Because the error state estimation algorithms are formulated in state-space form, the IMU error models will also be in state-space form. The inputs are modeled as independent Gaussian white noise processes. The challenge is to construct these models such that they have the same output statistical characteristics (i.e., Allan variance) as the IMU.

Note that such stochastic state-space models are not unique. In fact, this article is not intended to propose a particular model; although a specific ASD plot is discussed and a model is given as a tutorial example. Instead, the goal of this article is to present clearly the approach that is used or hinted at (with various specific models) in various articles, books [9], and standards [30], [28], [29]. The authors view the many flavors of this approach as the industry-standard. Unfortunately, most publications describing the method are not publicly available.

From a high-level, an outline of the method is as follows: (1) A continuous-time state-space model is constructed using information from the AV/ASD plot. (2) The continuous-time

IMU stochastic model is transformed to an equivalent discrete-time model. (3) The discrete-time model is used in simulation to produce data from which an ASD plot is produced for comparison with the instrument's ASD plot. (4) When the designer is satisfied with the IMU error model, it is appended to the vehicle state error model and used for the design of the INS error state estimator.

III. BACKGROUND

Because the manufacturer supplied AV/ASD information is the starting point for the stochastic error model development, this section reviews the Allan Variance and its relationship to the power spectral density. A brief history of the AV is included in the sidebar entitled "A Brief Historical Review of the Allan Variance".

A. Allan Variance

The Allan Variance is a well-known time domain analysis technique that was originally developed to characterize and study the frequency stability of oscillators [48], [49], [50]. Due to its relative simplicity, it has been successfully adopted to communicate IMU performance specification and to characterize their stochastic errors [28], [29], [32], [34], [36], [39], [43], [44], [46], [47].

Given a set of data, the process for computing the Allan Variance is as follows. Let $D = \{\tilde{u}_i\}_{i=1}^L$ be a (detrended) set of specific force (or angular rate) data, measured at a constant sampling interval T for a stationary (i.e., motion isolated) IMU. For each $n \in [1, L/2]$, the AV is computed for values of the cluster time $\tau = nT$ ranging from T to $LT/2$. For a given n , at each time instant $t_i \in [T, 2T, \dots, (L-n)T]$, a group of n consecutive data points (beginning at t_i) form a cluster: $\{\tilde{u}_j\}_{j=i}^{i+n-1}$. The average value is computed for each such n -point cluster, $\bar{u}_i(\tau) = \frac{1}{n} \sum_{j=0}^{n-1} \tilde{u}_{i+j}$. Then the AV for duration τ is computed as the average of the $(L-2n)$ squared cluster differences [28], [49]:

$$\hat{\sigma}_u^2(\tau) = \frac{1}{2(L-2n)} \sum_{i=1}^{L-2n} [\bar{u}_{i+n}(\tau) - \bar{u}_i(\tau)]^2. \quad (12)$$

Since some IMUs (especially those that are high-grade) provide the integral of specific force (or angular rate), denoted as $\tilde{\theta}_i$, we may alternatively define $\bar{u}_i(\tau)$ as

$$\bar{u}_i(\tau) = \frac{\tilde{\theta}_{i+n} - \tilde{\theta}_i}{\tau} \quad (13)$$

Substitution of eqn. (13) in eqn. (12) yields,

$$\hat{\sigma}_u^2(\tau) = \frac{1}{2\tau^2(L-2n)} \sum_{i=1}^{L-2n} (\tilde{\theta}_{i+2n} - 2\tilde{\theta}_{i+n} + \tilde{\theta}_i)^2 \quad (14)$$

which is an alternative formula for computing the AV [28].

For graphical analysis, the square root of the AV, $\hat{\sigma}_u(\tau)$, called the Allan Standard Deviation (ASD), is typically plotted on a log-log scale with cluster time τ along the horizontal axis. Due to the finite length of dataset D , the number of clusters with duration τ

will decrease as τ increases; therefore, the standard deviation of the computed ASD, $\hat{\sigma}_u(\tau)$, increases with n (or τ) as [51], [52]:

$$\sigma[\hat{\sigma}_u(\tau)] = \kappa \sqrt{\frac{n}{L}} \hat{\sigma}_u(\tau) \quad (15)$$

where κ is an empirical constant, generally approximated as $\kappa \approx 1/\sqrt{2}$, for IMU error analysis [53], [28], [29], [34], [54].

B. PSD and Allan Variance

The AV is related to the two-sided power spectral density by,

$$\sigma_u^2(\tau) = 4 \int_0^\infty S_u(f) \frac{\sin^4(\pi f \tau)}{(\pi f \tau)^2} df. \quad (16)$$

The text following eqn. (C.1) in IEEE Standard 952-1997 [28] interprets this equation as the Allan variance being proportional to the total noise power in the signal u when passed through a transfer function that is determined by the method that is used to create and operate on the clusters. The derivation of eqn. (16) can be found on p. 79 in [55]. There is no inversion formula for eqn. (16) (e.g., see [53]). In this expression, $S_u(f) = S_u(s)|_{s=j2\pi f}$ where $s \in \mathbb{C}$ is the Laplace variable, $j = \sqrt{-1}$, and $f \in \mathbb{R}$ has units of Hertz.

C. Modeling via Independent Noise Sources

When the power spectrum is represented as a power series in frequency f , it has the form,

$$S_u(f) = \dots + N^2 + \frac{B^2}{2\pi f} + \frac{K^2}{(2\pi f)^2} + \dots \quad (17)$$

This form of the PSD is convenient. By the principle of superposition, it corresponds to the power spectrum of the signal

$$u(t) = \dots + z_N(t) + z_B(t) + z_K(t) + \dots \quad (18)$$

where the signals $z_N(t)$, $z_B(t)$, $z_K(t)$, etc. are mutually independent, zero mean, noise processes. With this assumption, applying eqn. (16) to eqn. (17), yields an AV with the form

$$\sigma_u^2(\tau) = \dots + \sigma_{z_N}^2(\tau) + \sigma_{z_B}^2(\tau) + \sigma_{z_K}^2(\tau) + \dots, \quad (19)$$

where the specific functional form of each AV term can be computed and is available in various sources [28], [29], [30], [34], [55]. The functional form of each AV term is easily associated with a portion of the ASD graph.

The "Continuous-Time State-Space Models" section describes the method for making this association and defining continuous-time state-space models for each term. The state-space model for each term is driven by its own independent, Gaussian, white, driving noise resulting in each signal (e.g., $z_N(t)$, $z_B(t)$, $z_K(t)$) being mutually independent. These state-space models can be exact for the terms that correspond to even functions of f in eqn. (17). However, as previously stated and as exemplified in a sidebar, the power spectrum terms that are odd functions of the frequency f , for example the term $\frac{B^2}{2\pi f}$, cannot be exactly modeled by any finite dimensional, linear, state-space model; therefore, these terms must be approximately modeled, carefully balancing trade-offs that are discussed later.

Any number of terms may be included in the power series representation of eqn. (17). This results in the same number of

terms in the signal model of eqn. (18) and the AV model of eqn. (19). Each term represents a different type of noise coming from an independent source. The typical shape of the ASD graph is depicted in Fig. 3 with five independent noise sources (See also Fig. C.8 in [28]). In the ASD plot, each noise type is associated with a characteristic slope that facilitates identification of that noise type and its model parameters. Not all noise types are evident in each instrument. When present, the model parameters and range of τ over which the noise term is dominant may be different for each instrument.

The N , B , and K terms are typically dominant in commercial-grade IMU's (e.g., see Fig. 1 and 2). Instrument design choices (e.g., quantization approach, and sample period) cause the stochastic error to appear as white noise for small τ . This white noise is accounted for in the random walk noise term (i.e., N). However, the stochastic error is not truly white. As the cluster time τ increases the ASD plot may exhibit bias instability (B), rate random walk (K), and other noise types. For the ASD plot to exhibit these other noise types, the IMU data set used to generate the ASD plot must be very long. When the INS is designed to work with aiding measurements that are expected to occur frequently (e.g., several times per minute), the state estimator will have the aiding information that it needs to maintain the INS calibration in real-time, when those aiding measurements are available. The ASD plot out to several minutes (e.g., hundreds of seconds) is of interest for analyzing performance during intervals when the aiding measurements are not available; however, the specific shape of the ASD curve for very large τ is typically not of interest.

Columns one and two of Table I include the specific names of the N , B , and K noise terms for gyros and accelerometers. Columns three and four of Table I summarize the relationships between the Allan Variance and PSD for these noise types, as derived in [28], [34]. The N , B , and K terms will be the focus of the discussion in the "Continuous-Time State-Space Models" section. The underlying ideas of the approach extend to other types of noise, when the ASD for a particular instrument, exhibits them.

IV. CONTINUOUS-TIME STATE-SPACE MODELS

This section considers the development of continuous-time state-space models able to reproduce (approximately) ASD plots

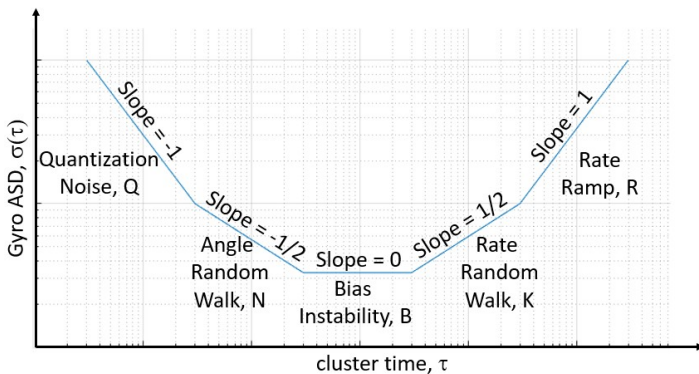


Fig. 3. Typical gyro ASD shape corresponding to eqns. (17-19).

and the power spectral density of eqn. (17). Throughout, the ideas will be illustrated using the example ASD in Fig. 2. Fig. 1 will only be discussed with reference to the B and K terms. The overall model will have the form,

$$z(t) = z_N(t) + z_B(t) + z_K(t). \quad (20)$$

where $z_N(t)$, $z_B(t)$ and $z_K(t)$ are the IMU stochastic error signals associated with coefficients N , B , and K , respectively.

A. Random Walk Errors: Angular and Velocity: $z_N(t)$

The PSD term N^2 in eqn. (17) is constant with respect to frequency f , which corresponds to the power spectrum of white noise [56]. Therefore,

$$z_N(t) = \omega_N(t) \quad (21)$$

where $\omega_N(t)$ is white Gaussian random noise with power spectral density

$$S_N = N^2. \quad (22)$$

In the literature and on manufacturer specifications, this type of error is called *angular random walk* error for gyros and *velocity random walk* error for accelerometers.

Applying the transformation in eqn. (16) to $S_{z_N}(f) = N^2$ yields [28],

$$\sigma_{z_N}^2(\tau) = \frac{N^2}{\tau} \quad \text{or} \quad \sigma_{z_N}(\tau) = \frac{N}{\tau^{1/2}}. \quad (23)$$

which is summarized in the corresponding row of Table I. This shows that, on an ASD plot, angular/velocity random walk will be represented by a line with a slope of $-\frac{1}{2}$, as shown in Fig. 4.

The value of the random walk parameter N can be approximately determined from the manufacturer supplied ASD plot. This is accomplished by identifying the range of τ on the ASD plot that has a slope of $-\frac{1}{2}$ and drawing a line tangent to it. In Fig. 2, a red dashed tangent line is drawn for $\tau \in [0.01, 30]$ seconds. From eqn. (23), it is clear that $\sigma_{z_N}(\tau)|_{\tau=1} = N$. Therefore, the value of N can be extracted from the ASD plot as the value of the tangent line (with slope of $-\frac{1}{2}$) at $\tau = 1$ s. For the example of Fig. 2, the result is $N \approx 0.0033$ m/s^{3/2}.

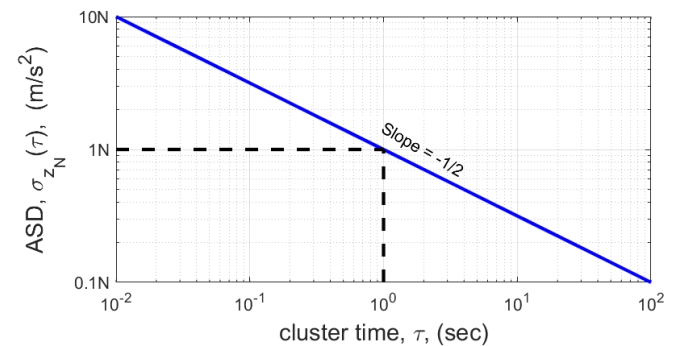


Fig. 4. Angular/Velocity random walk ASD plot. See eqn. (23).

B. Random Walk Errors: Rate and Acceleration: $z_K(t)$

The term $\frac{K^2}{(2\pi f)^2} = \frac{K}{s} \frac{K}{s^*} \Big|_{s=j2\pi f}$ in eqn. (17) corresponds to a linear system with transfer function $T(s) = \frac{1}{s}$. A state-space model is

$$\dot{z}_K(t) = \omega_K(t), \quad (24)$$

where $z_K(t)$ is the output and the input $\omega_K(t)$ is white Gaussian noise with power spectral density

$$S_K = K^2. \quad (25)$$

In the literature and on manufacturer specifications, this type of error is called *rate random walk* error for gyros and *acceleration random walk* error for accelerometers.

Given eqns. (24) and (25), the PSD of $z_K(t)$ is,

$$S_{z_K}(f) = \left(T(s)T(s^*) \Big|_{s=j2\pi f} \right) K^2 = \frac{K^2}{(2\pi f)^2}, \quad (26)$$

which has the desired form corresponding to the third term in eqn. (17). Using eqn. (16) on this $S_{z_K}(f)$ yields [28],

$$\sigma_{z_K}^2(\tau) = \frac{K^2\tau}{3} \quad \text{or} \quad \sigma_{z_K}(\tau) = K\sqrt{\frac{\tau}{3}} \quad (27)$$

which is summarized in the corresponding row of Table I. Eqn. (27) shows that on an ASD plot the rate/acceleration random walk error will be represented by a line with a slope of $+\frac{1}{2}$, as shown in Fig. 5.

The rate/acceleration random walk parameter K can be approximately determined from the manufacturer supplied ASD plot. The first step is to identify the range of τ on the ASD plot that has a slope of $+\frac{1}{2}$ (if it exists) and draw a line tangent to it. In Fig. 2, the dashed black line drawn for $\tau \in [3, 500]$ seconds, has slope $+\frac{1}{2}$ and is approximately tangent to the ASD curve at values of $\tau \geq 100$ seconds. Because τ is large, this portion of the ASD plot usually has a higher degree of uncertainty, as discussed relative to eqn. (15). The second step uses the tangent line to estimate K . From eqn. (27), it is clear that $\sigma_{z_K}(\tau)|_{\tau=3} = K$; therefore, an easy way to estimate the value of K from the ASD plot is to find the value of the straight line approximation when $\tau = 3$ s. In the

example of Fig. 2, depending on how the analyst determines the straight-line approximation, $K \approx 0.00014$ m/s^{5/2}.

Based on the ASD plots in Fig. 1, for cluster times up to 1000 seconds, the gyros in the μ Nav unit may not require inclusion of angular rate random walk noise.

C. Cumulative Error Model: N, K

Since the angular random walk and rate random walk errors (or velocity random walk and acceleration random walk errors) each have even power spectra, it was straightforward to establish state-space models able to reproduce the corresponding terms in the power spectrum and their portions of the ASD plot.

Based on the two previous sections, the state-space model would be,

$$\dot{z}_K(t) = \omega_K(t) \quad (28)$$

$$z_{NK}(t) = z_N(t) + z_K(t) \quad (29)$$

where $z_N(t) = \omega_N(t)$ is white random noise with PSD N^2 , $\omega_K(t)$ is a white random noise with PSD K^2 , and $\omega_N(t)$ and $\omega_K(t)$ are independent, which results in $z_N(t)$ and $z_K(t)$ being independent. The ASD for this model is,

$$\sigma_{NK}^2(\tau) = \frac{N^2}{\tau} + \frac{K^2\tau}{3}. \quad (30)$$

The ASD plot for this model, using the values $N = 0.0033$ m/s^{3/2} and $K = 0.00014$ m/s^{5/2} is shown in Fig. 2 as the solid green line.

D. Bias Instability: $z_B(t)$

Some ASD plots, such as those in Fig. 1 do not exhibit the $+1/2$ slope associated with $z_K(t)$, but do have a wide flat region for larger values of τ . This flat region cannot be well modeled by either the N or K terms. For other instruments, the ASD plot may exhibit a wide and flat portion between the values of τ corresponding to the N and K regions. In this case, the AV (and ASD) in eqn. (30) for the NK -model may be too small in this middle range of τ . In either of these circumstances, there is sufficient bias instability that performance may be improved by accounting for it in the model.

The error term $z_B(t)$ corresponding to $S_{z_B}(f) = \frac{B^2}{2\pi f}$ is generally referred to, in the literature, as the *bias instability* (or flicker noise) [28], [29], [34], [44], [39]. Applying eqn. (16) to $S_{z_B}(f) = \frac{B^2}{2\pi f}$ for $f \leq f_0$ (and 0 otherwise) yields [28],

$$\sigma_{z_B}^2(\tau) = \frac{2B^2}{\pi} \left[\ln(2) - \frac{\sin^3(x)}{2x^2} (\sin x + 4x \cos x) + Ci(2x) - Ci(4x) \right] \quad (31)$$

where $x = \pi f_0 \tau$, Ci is the cosine integral function [57], and the parameter f_0 is defined as the cut-off frequency [28].

The ASD plot for bias instability is shown in Fig. 6. The figure shows that $\sigma_{z_B}(\tau)$ grows for small τ reaching a plateau for $\tau > \frac{1}{f_0}$. Therefore, the value of $\tau \approx \frac{1}{f_0}$ defines the portion of the ASD plot for which the bias instability (or flicker noise) contributes its maximum value to the SD plot. In this region, it is possible to

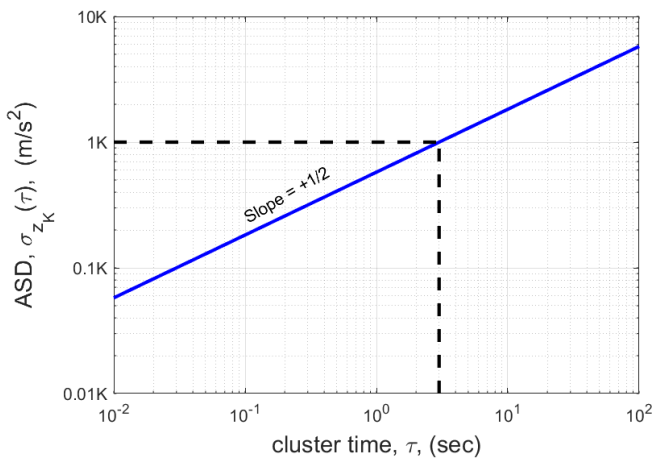


Fig. 5. Rate/Acceleration random walk ASD plot. See eqn. (27).

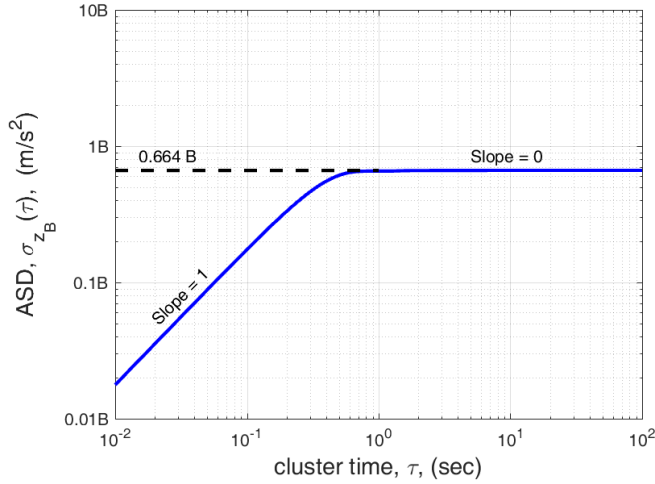


Fig. 6. Bias instability ASD plot for eqn. (31) with $f_0 = 1$.

show that the sine and cosine terms in eqn. (31) approach zero, so that, in the flat region,

$$\sigma_{z_B}^2(\tau) \approx \frac{2B^2 \ln(2)}{\pi} \quad \text{or} \quad \sigma_{z_B}(\tau) \approx 0.664B. \quad (32)$$

These equations provide a simple method for extracting an approximate value of B from the ASD plot. In this approach (see e.g., p. 6 in [35], p. 21 in [44], p. 10 in [54], p. 114 in [55]), as can be inferred from Section B.4.5 in [28], the value of B would be selected so that $\frac{2B^2 \ln(2)}{\pi}$ approximates the plot of $\sigma_z^2(\tau)$ for the values of τ for which the ASD plot is flat. For the ASD plot in Fig. 1, the cyan horizontal lines approximate the minimum ASD values of $9.5e-3$ and $1.40e-2$ deg/s, which correspond to values of B between $1.43e-2$ and $2.11e-2$ deg/s. For the ASD plot in Fig. 2, the minimum ASD value of $7.4e-4$ m/s² corresponds to $B = 1.11e-3$ m/s².

Because the power spectrum of the bias instability term, $\frac{B^2}{2\pi f}$, is not an even power of $s = j2\pi f$, there is no finite-order linear state-space model that fits it exactly. As a consequence, the navigation system designer must select a state-space model to approximate the bias instability error effects. This is somewhat of an art, as each IMU is distinct, each application has different specifications, and each designer may have different ideas about suitable models and trade-offs.

Various methods have been suggested in the literature to approximately account for the bias instability. These include first-order Gauss-Markov [4], [32], [36], [39], [44], [58] and higher-order autoregressive models [43], [46], [47]. One important trade-off is that, as the dimension of the state-space model increases, the fidelity of the approximation may increase, but so does the required real-time computational load of the state estimation algorithm. In addition, more elaborate models may not be robust to unmodeled dynamics and nonlinearity, especially when some added states are weakly observable. These topics are analyzed further in the “Discussion of Issues and Trade-offs” section.

To exemplify the idea, the next section considers a first-order Gauss-Markov model, which represents exponentially correlated noise, to model the bias instability error.

E. Gauss-Markov Error Model

A first-order continuous-time Gauss-Markov model has the following form [9], [56],

$$\dot{z}_G(t) = -\mu_B z_G(t) + \omega_B(t) \quad (33)$$

with,

$$\mu_B = \frac{1}{T_B}, \quad \text{where } T_B > 0. \quad (34)$$

The symbol T_B represents the correlation time of the process. The symbol $\omega_B(t)$ represents a white driving noise with power spectral density S_B .

The transfer function corresponding to eqn. (33) is,

$$T(s) = \frac{1}{s + \mu_B},$$

which yields the PSD,

$$S_{z_G}(\omega) = \frac{S_B}{\omega^2 + \mu_B^2}.$$

Applying eqn. (16) to $S_{z_G}(s)$, yields [28],

$$\sigma_{z_G}^2(\tau) = \frac{S_B T_B^2}{\tau} \left[1 - \frac{T_B}{2\tau} \left(3 - 4e^{-\frac{\tau}{T_B}} + e^{-\frac{2\tau}{T_B}} \right) \right]. \quad (35)$$

A plot of $\sigma_{z_G}(\tau)$ is shown in Fig. 7. Some special cases are worthy of note.

- For smaller cluster times, where $\tau \ll T_B$,

$$\sigma_{z_G}^2(\tau) \approx \frac{S_B \tau}{3}, \quad (36)$$

so that the ASD plot has a slope of $+\frac{1}{2}$ for small τ .

- When $\tau = 1.89 T_B$,

$$\sigma_{z_G}^2(1.89 T_B) = (0.4365 \sqrt{S_B T_B})^2 \quad (37)$$

or $\sigma_{z_G}(1.89 T_B) = 0.4365 \sqrt{S_B T_B}$.

- For larger cluster times, where $\tau \gg T_B$,

$$\sigma_{z_G}^2(\tau) \approx \frac{S_B T_B^2}{\tau} \quad (38)$$

so that the ASD plot has a slope of $-\frac{1}{2}$ for large τ .

The first-order scalar Gauss-Markov process can be used (approximately) to model the flat portion (i.e., bias instability) of the ASD plot.

If the manufacturer only provides the values of B and T_B , then the value of μ_B can be computed using eqn. (34). The value of

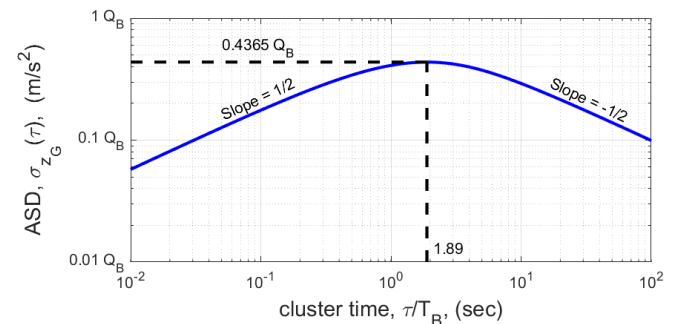


Fig. 7. Gauss Markov ASD plot defined in eqn. (35) with $q_B = \sqrt{S_B T_B}$.

S_B is selected by setting $\sigma_{z_B}^2$ from eqn. (32) equal to $\sigma_{z_G}^2$ as given by eqn. (37), and solving for S_B :

$$S_B = \frac{2 B^2 \ln(2)}{\pi(0.4365)^2 T_B}. \quad (39)$$

With μ_B and S_B known, the state-space model of eqn. (33) is completely specified.

If instead, the manufacturer provides the ASD plot, and the bias instability is significant enough to warrant inclusion in the model, then the analyst can first select T_B so that $1.89 T_B$ lies near the flat portion of the ASD plot. Then, choose S_B so that $\sigma_{z_G}(1.89 T_B)$, as defined in eqn. (37), approximates the flat region of the ASD plot. For the ASD plot in Fig. 2, the minimum value is $7.4e-4 \text{ m/s}^2$ at $\tau = 60\text{s}$. These values correspond to $T_B = 31.7\text{s}$, $S_B = 9.0e-8 \text{ m}^2/\text{s}^5$, and $B = 1.11e-3 \text{ m/s}^2$.

F. Cumulative Error Model: N , B , K

Consider the two-state state-space model structure, where $z(t)$ is modeled by eqn. (20), $z_N(t)$ is modeled by eqn. (21), $z_K(t)$ is modeled by eqn. (24), and the bias instability term in eqn. (20) is modeled by $z_B(t) = z_G(t)$ as defined in eqn. (33). This yields a two-state model in the form of eqns. (6-7) with,

$$A_z = \begin{bmatrix} -\mu_B & 0 \\ 0 & 0 \end{bmatrix}, \quad B_z = \begin{bmatrix} 1 & 0 \\ 0 & 1 \end{bmatrix}, \quad C_z = [1 \quad 1] \quad (40)$$

where $\vec{x}_z(t) = [z_G(t), z_K(t)]^\top$, $\vec{\omega}_z(t) = [\omega_B(t), \omega_K(t)]^\top$, and $\eta_z(t) = \omega_N(t)$. The continuous-time process noise PSD matrix S_{ω_z} of $\vec{\omega}_z$ is,

$$S_{\omega_z} = \begin{bmatrix} S_B & 0 \\ 0 & S_K \end{bmatrix} \quad (41)$$

and the measurement noise PSD is $S_{\eta_z} = S_N$.

The ASD for this state-space model is

$$\sigma_z(\tau) = (\sigma_{z_N}^2(\tau) + \sigma_{z_G}^2(\tau) + \sigma_{z_K}^2(\tau))^{1/2} \quad (42)$$

where the three ASD terms on the right are defined in eqns. (23), (27), and (35).

Fig. 8 builds on the ASD plot in Fig. 2. The data (blue x's) and K and N tangent lines are the same. Fig. 8 also shows the ASD of eqn. (42) using the two sets of parameters as summarized in the second and third rows of Table II (i.e., Untuned and Manually Tuned).

The untuned parameters from the second row of the table are those stated at the end of the ‘‘Gauss-Markov Error-Model’’ section. These values result in the green dashed curve, which is clearly too high in the region of the curve near its minimum. The suggested approaches stated above for choosing N , B , and K

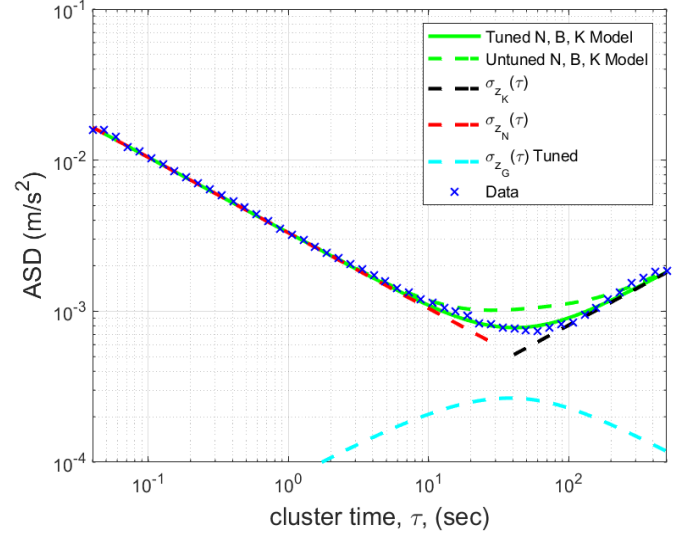


Fig. 8. ASD from Fig. 2 along with ASD plots for N , B and K .

independently, neglect the fact that for each τ the AV for each type of noise is additive:

$$\sigma_z^2(\tau) = \sigma_{z_N}^2(\tau) + \sigma_{z_B}^2(\tau) + \sigma_{z_K}^2(\tau). \quad (43)$$

Therefore, the parameters N , B , K , and T_B should instead be adjusted jointly so that the three term AV (or ASD) model, fits the ASD plot for the instrument data. Manually adjusting the values of T_B and B to those in the third row of Table II results in the solid green curve, which is a better fit. An optimization-based approach to selecting the parameters is discussed in the subsection entitled ‘‘Optimization-based Parameter Selection for a Given Model’’.

Fig. 8 includes the curve for the Gauss-Markov ASD of eqn. (35) plotted as a cyan dashed line, using the tuned values of T_B and S_B .

G. Summary

Many alternative choices for the structure of the state-space model exist: no states, just z_N ; a single state z_G and z_N ; a single state z_K and z_N ; generalizations of the above two-state model; plus, higher dimensional models. Various trade-offs related to selection of the structure of the state-space model are discussed in the ‘‘Discussion of Issues and Trade-offs’’ section.

V. DISCRETE-TIME EQUIVALENT MODEL

The previous section has discussed the process of determining a continuous-time state-space model with the form of eqns. (6-7) to approximate the IMU error characteristics as quantified by the ASD (or power spectrum) plot. Since the INS and EKF are implemented in discrete-time, the state-space IMU error model needs to be transformed to the equivalent discrete-time form,

$$\vec{x}_z(k+1) = \Phi \vec{x}_z(k) + \vec{\omega}_z(k), \quad (44)$$

$$z(k) = H \vec{x}_z(k) + \eta(k) \quad (45)$$

where discrete-time k index corresponds to continuous-time $t = kT$, $\vec{\omega}_z(k) \sim N(0, Q_{z_d})$ is a white Gaussian random variable

TABLE II

EXTRACTED AV PARAMETERS RELATED TO FIG. 8

Coef.	N	B	K	T_B
Untuned Value	0.0033	0.0011	0.00014	32
Manually-tuned Value	0.0033	0.0004	0.00014	20
Optimization-based Value	0.0033	0.0001	0.00012	50
Unit	$\text{m/s}^{3/2}$	m/s^2	$\text{m/s}^{5/2}$	s

with covariance Q_{z_d} , and $\eta(k) \sim N(0, Q_{\eta_d})$ is a white Gaussian random variable with covariance Q_{η_d} . The processes $\vec{\omega}_z(k)$ and $\eta(k)$ are independent. Within this article, *equivalent* means that the continuous-time and discrete-time stochastic error models produce the same first and second order statistics at the IMU sampling times.

The following subsections describe how to compute the discrete-time model parameters (Φ , Q_{z_d} , H , Q_{η_d}), that are required for the discrete-time estimator implementation, from the continuous-time model parameters (A_z , B_z , S_{ω_z} , S_{η_z} , C_z).

A. Discrete-Time Equivalent to Eqn. (6)

The process of transforming the continuous-time model of eqn. (6) to the discrete-time state-space model of eqn. (44) is described in various references (e.g. Section III.D in [59] or Section 4.7 of [3]), with,

$$\Phi = e^{A_z T}, \text{ and} \quad (46)$$

$$Q_{z_d} = \int_0^T \Phi(T, s) B_z S_{\omega_z}(s) B_z^T \Phi(T, s)^T ds, \quad (47)$$

where $T = t_k - t_{k-1}$ is the IMU sampling interval and $\Phi(T, s) = \exp(A_z(T - s))$. Both Φ and Q_{z_d} can be computed simultaneously using a method by Van Loan [60], as described in Appendix I of [59].

Depending on the method used to model the bias instability and the state definition, the A_z matrix in the continuous-time state-space model may have various forms. For the Cumulative N - B - K Error Model with the discrete-time state vector, $\vec{x}_z(k) = [z_G(k), z_K(k)]^T$, the A_z matrix in eqn. (40) transforms to,

$$\phi = \begin{bmatrix} e^{-\mu_B T} & 0 \\ 0 & 1 \end{bmatrix}. \quad (48)$$

Since A_z and S_{ω_z} are constant and diagonal, and B_z is the identity, (47) simplifies to,

$$\begin{aligned} Q_{z_d} &= \begin{bmatrix} S_B \int_0^T \exp(-2\mu_B(T-p)) dp & 0 \\ 0 & S_K T \end{bmatrix} \\ &= \begin{bmatrix} \frac{S_B}{2\mu_B} (1 - e^{-2\mu_B T}) & 0 \\ 0 & S_K T \end{bmatrix}. \end{aligned} \quad (49)$$

Because $T \ll T_B$ and $\mu_B = \frac{1}{T_B}$, after expanding the exponential term it is clear that,

$$Q_{z_d} \approx S_{\omega_z} T = \begin{bmatrix} S_B T & 0 \\ 0 & S_K T \end{bmatrix}. \quad (50)$$

B. Discrete-Time Equivalent to Eqn. (7)

The objective of this section is to determine an equivalent discrete-time measurement model having the form of eqns. (44-45) that is equivalent to eqn. (6-7).

Because the method of the previous section was designed such that eqns. (6) and (44) produce the same first and second order statistics for the state, it is the case that $H = C_z$. The only item left for consideration is to determine how to compute the covariance Q_{η_d} from the PSD S_N so that the overall effect (in terms of the first two moments) of $z(k)$ on the integrated state

in the augmented state-space model is the same as that of $z(t)$ at the sampling periods.

Using the principle of superposition, assume that the driving noise terms $\omega_B(t)$ and $\omega_K(t)$ (and therefore $\omega_z(t)$) are zero and that the covariance of the initial conditions is zero; so that the only remaining non-zero error is $\eta_z(t)$, which equals $\omega_N(t) = z_N(t)$ according to the model in eqns. (21) and (40). Consider the simple case where the kinematic model of eqn. (1) is,

$$\dot{x}_v(t) = u(t). \quad (51)$$

This could, for example, correspond to u being an angular rate (or acceleration) measurement and x_v representing the angle (or velocity). In continuous-time, the navigation system would use the measurement $\tilde{u}(t)$ to compute $\hat{x}_v(t)$,

$$\dot{\hat{x}}_v(t) = \tilde{u}(t). \quad (52)$$

With the assumptions stated at the beginning of the paragraph,

$$\tilde{u}(t) = u(t) + \eta_z(t). \quad (53)$$

Define the error signal, $e(t) = x_v(t) - \hat{x}_v(t)$. Based on eqns. (51-53),

$$\dot{e}(t) = -\eta_z(t), \quad (54)$$

where according to eqn. (21-22) the PSD of $\eta_z(t) = \omega_N(t)$ is S_N . In this special case, $e(t)$ is a continuous-time random walk process. Due to the assumption that the initial covariance of $e(t)$ is zero (i.e., $\text{cov}(e(0)) = P_e(0) = 0$), the covariance function (i.e., $\text{cov}(e(t)) = P_e(t)$) is

$$P_e(t) = S_N t \text{ for any } t \geq 0. \quad (55)$$

This result is derived in many textbook discussions of the continuous-time random walk processes, see e.g., the discussion of eqn. (4.85) in [3].

The discrete-time model that is equivalent to eqn. (51) is

$$x_v(k+1) = x_v(k) + u(k)T. \quad (56)$$

The discrete-time model that is equivalent to eqn. (52) is

$$\hat{x}_v(k+1) = \hat{x}_v(k) + \tilde{u}(k)T. \quad (57)$$

Given the discrete-time measurement model,

$$\tilde{u}(k) = u(k) + \eta(k), \quad (58)$$

where $\text{cov}(\eta(k)) = Q_{\eta_d}$ as defined in eqn. (45), the error signal $e(k) = x_v(k) - \hat{x}_v(k)$ has the time propagation model

$$e(k+1) = e(k) - \eta(k)T. \quad (59)$$

In this special case, $e(k)$ is a discrete-time random walk process. Eqn. (59) allows computation of the discrete-time error covariance caused by $\eta(k)$ (i.e., $P_e(k) = \text{cov}(e(k))$) as

$$P_e(k+1) = P_e(k) + T^2 Q_{\eta_d} \text{ for any } k \geq 0 \quad (60)$$

where Q_{η_d} is defined in eqn. (45). Due to the assumption that the initial covariance of $e(k)$ is zero,

$$P_e(k) = k T^2 Q_{\eta_d} \text{ for any } k \geq 0. \quad (61)$$

Given the equivalence objective stated in the first sentence of this section, the continuous and discrete time must result in the

same values for the error covariance at the discrete sample times. Equating the covariance of the continuous-time and discrete-time random walk error processes at the sampling times – i.e., setting eqn. (55) equal to eqn. (61) – yields,

$$\begin{aligned} P_e(t)|_{t=kT} &= P_e(k) \\ S_N k T &= k T^2 Q_{\eta_d}. \end{aligned}$$

which provides the equation (see also the “Discussion of Eqn. (62)” sidebar):

$$Q_{\eta_d} = \frac{S_N}{T}. \quad (62)$$

This equation relates the covariance Q_{η_d} of the discrete-time IMU measurement noise (needed for the state estimator design) to the PSD S_N of the continuous-time measurement noise (derived from the ASD plot). Substituting eqn. (62) into eqn. (61) shows that the covariance of the integrated error signal ($e(k)$) increases linearly with time in proportion to the PSD S_N , as is expected for a random walk.

Together, eqns. (46-47), (62), and $H = C_z$ are the conversions needed to transform the continuous-time state-space error model to its equivalent discrete-time error model as necessary for the EKF design.

VI. ASD VERIFICATION OF THE STATE-SPACE MODEL

The previous sections have presented methods to develop continuous and discrete-time state-space models to approximate the IMU stochastic errors as characterized by the AV method. If the method that a designer uses is valid, then data generated by the discrete-time state-space model should result in an ASD plot that closely approximates the ASD plot provided by the IMU manufacturer. This section contains an example to demonstrate this verification process.

The example starts from the ASD plot of Fig. 2. The model, parameter selection and data generation methods are as follows:

- 1) The AV parameters are extracted from the ASD plot using the method described in the “Continuous-Time State-Space Models” section. The parameters for this example are stated in the third row of Table II (i.e., manually tuned).
- 2) The value of $\mu_B = \frac{1}{T_B} = 0.05 \text{ s}^{-1}$ by eqn. (34), $S_B = 1.8528e-8 \text{ m}^2/\text{s}^5$ by eqn. (39), and $S_K = 1.9600e-8 \text{ m}^2/\text{s}^5$ by eqn. (25). By eqn. (41),

$$S_{\omega_z} = \begin{bmatrix} 1.8528e-8 & 0.00 \\ 0.00 & 1.9600e-8 \end{bmatrix}.$$

For A_z , B_z , and C_z defined as in (40), using eqns. (48) and (49)

$$\Phi = \begin{bmatrix} 0.9995 & 0 \\ 0 & 1 \end{bmatrix} \text{ and } Q_{z_d} = \begin{bmatrix} 1.853e-10 & 0 \\ 0 & 1.960e-10 \end{bmatrix}.$$

- 3) Using eqn. (22), the continuous-time measurement noise PSD is $S_N = 1.089e-5 \text{ m}^2/\text{s}^3$. Using eqn. (62), the discrete-time measurement noise covariance is $Q_{\eta_d} = 1.089e-3 \text{ m}^2/\text{s}^4$.
- 4) Starting from an initial condition of zero, the state vector $\tilde{x}_z(k)$ is propagated using eqn. (44) and the IMU error $z(k)$ is computed using eqn. (45). The data frequency is 100 Hz

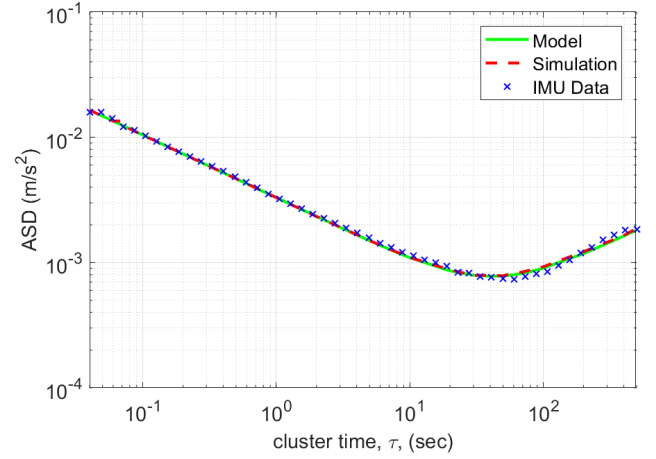


Fig. 9. ASD plot for IMU data (blue x’s), model defined by eqn. (42), and simulated data as described in the “ASD Verification of the State-Space Model” section.

so that $T = 0.01 \text{ s}$. For simulation purpose, $L = 10^7$ data samples (or 10^5 s) were generated.

- 5) Fig. 9 shows the ASD plot for the simulated data as the red dashed curve. The blue x’s show the ASD curve for the IMU data, which is the same as is shown in Figs. 2 and 8. The green curve is the ASD for the analytic model as computed by eqn. (42), which is the same as is shown in Fig. 8.

The close match between the green and red curves verifies the continuous-time to discrete-time state-space model transformation. The closeness of the fit between those two curves and the actual ASD plot depends on the choice of the structure and parameters of the continuous-time state-space model.

VII. DISCUSSION OF ISSUES AND TRADE-OFFS

The previous sections presented an example approach to extract a discrete-time state-space model to approximate the IMU error characteristics as quantified by an ASD graph. There is no single correct method. This section discusses various related issues and trade-offs.

A. User-Acquired Data

When the manufacturer does not provide an ASD plot (or provides information that the designer considers insufficient), the designer may contemplate getting their own data with which to construct the ASD plots. This data acquisition process should only be considered with care after considering the appropriate technical specifications [28], [29].

The sensor model in eqn. (3) shows that the sensor reading is a function of deterministic parameters, stochastic errors, and the actual signal $u(t)$. The ASD plot is only intended to characterize the stochastic errors $z(t)$. The data acquisition set-up to acquire data to produce the ASD of the instrument must isolate the IMU from the environment well enough that the contributions to the measurement \tilde{u} from u are negligible. Under the best circumstances, this is done on the lowest subterranean floor of a building, with the instrument attached to a heavy mass on

a vibration isolation system. Less than optimal results can be expected for an instrument placed on a desk in an office on a higher floor, due to motion of the building, vibrations in the floor, etc.

B. Optimization-based Parameter Selection for a Given Model

Once the designer selects a model structure, it is possible to set-up an optimization problem to select the model parameters. See Section 12.11.4.1.2 in [28].

For example, given the state-space model structure described in the ‘‘Cumulative Error Model: N , B , K ’’ section, corresponding to eqn. (42), the ASD model is

$$\sigma_z^2(\tau) = \frac{S_N}{\tau} + \frac{S_B T_B^2}{\tau} \left[1 - \frac{T_B}{2\tau} \left(3 - 4e^{-\frac{\tau}{T_B}} + e^{-\frac{2\tau}{T_B}} \right) \right] + \frac{S_K \tau}{3}$$

which can be written using the (positive) parameter vector $\vec{\theta} = [S_N \ S_B \ S_K \ T_B]$ as

$$\sigma_z^2(\tau; \vec{\theta}) = \frac{\theta_1}{\tau} + \frac{\theta_2 \theta_4^2}{\tau} \left[1 - \frac{\theta_4}{2\tau} \left(3 - 4e^{-\frac{\tau}{\theta_4}} + e^{-\frac{2\tau}{\theta_4}} \right) \right] + \frac{\theta_3 \tau}{3}. \quad (63)$$

Using the known values of the computed $\hat{\sigma}_u^2(\tau_i)$ for $i = 1, \dots, L/2$ as plotted in the ASD plot, and the weights

$$w_i = \frac{1}{\sigma^2[\hat{\sigma}_u^2(\tau_i)]}$$

where $\sigma^2[\hat{\sigma}_u^2(\tau_i)]$ is the variance of the computed $\hat{\sigma}_u^2(\tau_i)$, approximated as [51]:

$$\sigma^2[\hat{\sigma}_u^2(\tau_i)] = (2\sigma[\hat{\sigma}_u(\tau_i)])^2$$

with $\sigma[\hat{\sigma}_u(\tau_i)]$ defined in eqn. (15), a cost function such as

$$C(\vec{\theta}) = \sum_{i=1}^L w_i (\hat{\sigma}_u^2(\tau_i) - \sigma_z^2(\tau_i; \vec{\theta}))^2 \quad (64)$$

can be optimized over positive values of $\vec{\theta}$. The functional form of $\sigma_z^2(\tau; \vec{\theta})$ in eqn. (63) is linear in three parameters and only nonlinear in one. Therefore, the nonlinear search is only over θ_4 . For each value of θ_4 , the other optimal parameter values can be explicitly computed.

The results of performing this optimization are shown in the fourth row of Table II. Note that the optimization-based approach has decreased the size of B , which can be interpreted as the bias instability errors being less important than thought by the designer who performed the manual tuning. This might motivate the designer to study whether the two-state N , B , K model actually provides performance improvement under application conditions relative to the one-state N , K model. The engineering art is to select the appropriate model structure that enables the state estimator to calibrate the IMU sufficiently well to achieve a specified performance given the implementation trade-offs for a particular application.

A few words of caution are appropriate regarding the interpretation of such optimization-based approaches to parameter selection. Note that ‘optimization-based’ is not necessarily ‘optimal’. This approach yields the parameter vector that minimizes a cost function for a given model structure and choice of weights. Different cost functions, weights, or a different model will yield

different ‘optimized’ model parameters. Also, many designers view the IMU in their application as not quite as good as the IMU that the manufacturer specified, therefore, their preference is to select the IMU stochastic error model to slightly overbound the specified AV plot rather than to optimally match that curve.

C. Observability: Where is the Bias?

It is often the case that one of the deterministic errors accounted for in eqn. (3) is a constant unknown bias b . For clarity of the discussion in this section, if all other deterministic errors are assumed to be zero, then eqn. (3) has the form

$$\tilde{u}(t) = u(t) + b + z(t). \quad (65)$$

The detrending process, mentioned before eqn. (12) in reference to the computation of the AV, estimates and removes a bias from the specific set of data used to create the ASD plot. Over a set of experiments, the variance of this ‘turn-on bias’ could be determined to have the value P_{b_0} . Because the IMU turn-on bias may change from one run to the next, the unknown portion is considered as a constant bias b with the differential equation

$$\dot{b}(t) = 0 \quad (66)$$

with the initial covariance $P_b(0) = P_{b_0}$ [3], [9], [56].

Nonetheless, the ASD plot may still dictate the inclusion of the state z_K with model

$$\dot{z}_K(t) = \omega_K(t), \quad (67)$$

with the PSD for $\omega_K(t)$ being $S_K = K^2$ and initial covariance $P_{z_K}(0) = \text{cov}(z_K(0)) = 0$.

Including both b and z_K in the augmented state vector is problematic, as can be concluded from a simple observability analysis. Assume for a moment the ideal situation where the signal $y(t) = \tilde{u}(t) - u(t)$ is available. Also, assume that $z(t) = z_K(t)$ (accounting for additional stochastic errors would not improve the observability of b and z_K), then eqns. (65-67) are equivalent to

$$\begin{bmatrix} \dot{b}(t) \\ \dot{z}_K(t) \end{bmatrix} = \begin{bmatrix} 0 & 0 \\ 0 & 0 \end{bmatrix} \begin{bmatrix} b(t) \\ z_K(t) \end{bmatrix} \quad (68)$$

$$y(t) = \begin{bmatrix} 1 & 1 \end{bmatrix} \begin{bmatrix} b(t) \\ z_K(t) \end{bmatrix} \quad (69)$$

where the noise $\omega_K(t)$ has been dropped because it is not relevant to an observability analysis. For this system the observability matrix is

$$\mathcal{O} = \begin{bmatrix} 1 & 1 \\ 0 & 0 \end{bmatrix} \quad (70)$$

which has rank equal to one. Further analysis shows that it is only possible to estimate the sum $b(t) + z_K(t)$ (see Example 3.19 in [3]). Alternative modeling approaches are discussed in the ‘‘Trade-offs in State Augmentation’’ section.

D. Computational Impact of Augmented States

The augmented state vector, as defined in eqn. (5), has dimension $n_x = n_v + n_d + n_z$. In the following discussion, we will consider the dimension of $\vec{x}_v \in \mathbb{R}^{n_v}$ as fixed and known, typically $n_v = 9$ (see eqn. (4)).

For IMU state augmentation, the designer must choose the definition and model structure for the deterministic and stochastic IMU error state vectors $\vec{x}_d \in \mathbb{R}^{n_d}$ and $\vec{x}_z \in \mathbb{R}^{n_z}$. Because there are three gyros and three accelerometers in the IMU, if n_g states are augmented per gyro and n_a states per accelerometer, then $(n_d + n_z) = 3(n_a + n_g)$. Therefore, $n_x = n_v + 3(n_a + n_g)$. Increasing the number of augmented states allows for a higher fidelity model, but comes with trade-offs. The computational load of the extended Kalman filter increases in proportion to n_x^3 (i.e., $O(n_x^3)$), see [5], [9], [56]. Also, the desired increase in performance expected to be gained with the additional computations may not be realized. For example, as the number of augmented states is increased, observability issues may arise. While it is clear that unobservable states increase the computational load without providing any performance improvement, it may be less clear that weakly observable states may cause the implementation to be less robust to unmodeled dynamics and nonlinearities.

E. Trade-offs in State Augmentation

In sensor fusion applications, the IMU measurements are not processed in the state estimation (e.g. Kalman filter) measurement update, instead they are treated as known inputs and considered during the time propagation of the state vector (see eqn. (2)).

To illustrate the trade-offs related to state augmentation for modeling stochastic IMU errors in such a filtering context, the differential equation for velocity shall be considered. In a navigation frame mechanization, this velocity differential equation is given by (see Section 11.24 in [3])

$$\dot{\vec{v}}_{eb}^n = \mathbf{C}_b^n \vec{f}_{ib}^b - (2\vec{\omega}_{ie}^n + \vec{\omega}_{en}^n) \times \vec{v}_{eb}^n + \vec{g}_l^n. \quad (71)$$

In this notation, $\vec{v}_{eb}^n \in \mathbb{R}^3$ is the velocity of the platform (i.e. body frame) with respect to Earth given in navigation frame coordinates, \mathbf{C}_b^n is the direction cosine matrix describing the rotation from body frame to navigation frame, $\vec{\omega}_{ie}^n$ is the Earth rotation rate, $\vec{\omega}_{en}^n$ is the platform transport rate, and \vec{g}_l^n is the local gravity vector. The axes of the navigation frame point in the directions north, east, and down. The axes of the body frame usually coincide with the sensitive axes of the IMU. The quantity \vec{f}_{ib}^b is the specific force vector, which is defined as the difference between platform acceleration and local gravity vectors. The accelerometer triad contained in the IMU provides measurements $\tilde{\vec{f}}_{ib}^b$ of this specific force, which – assuming no deterministic errors – relates to the true specific force via the stochastic error vector $\vec{z}_a \in \mathbb{R}^3$:

$$\tilde{\vec{f}}_{ib}^b = \vec{f}_{ib}^b + \vec{z}_a. \quad (72)$$

Each scalar component of the vector \vec{z}_a is modeled as in eqns. (6-7). Substituting eqn. (72) into (71) yields

$$\dot{\vec{v}}_{eb}^n = \mathbf{C}_b^n \tilde{\vec{f}}_{ib}^b - (2\vec{\omega}_{ie}^n + \vec{\omega}_{en}^n) \times \vec{v}_{eb}^n + \vec{g}_l^n - \mathbf{C}_b^n \vec{z}_a. \quad (73)$$

Consider two accelerometer error modeling scenarios:

- 1) If only velocity random walk errors would be considered (see the “Random Walk Errors: Angle and Velocity: $z_N(t)$ ” section), the Kalman filter state vector would not need to be augmented. The velocity random walk simply ends up as process noise in the Kalman filter system model without the need for additional states. This model could be accurate for small time durations (τ smaller than a few seconds for the IMU in Fig. 2), but would largely ignore the other sensor characteristics described by the corresponding ASD plot for larger τ . It would not allow the sensor fusion algorithm to calibrate the IMU (e.g., estimate and remove a bias) on the fly.
- 2) Using either the first-order Gauss-Markov error model (or the acceleration random walk model), would add one accelerometer ‘bias state’ per axis. In this case, the IMU stochastic error model can match the ASD plot out to several tens of seconds. The estimated bias state allows removal of the effect to the sensor bias (i.e., calibration).

For the second case, both options (i.e., the first-order Gauss-Markov error model or the acceleration random walk model) have their pros and cons. With an acceleration random walk model, the variance of the bias state grows linearly with time (i.e., without bound) during time intervals when the bias is not observable (see Section 4.6.3.2 in [3]). The physical inertial sensor bias is of course bounded. When the bias becomes observable through aiding measurement information and vehicle motion, the unrealistic growth of the bias variance may cause the estimator gain to be unreasonably large. With the Gauss-Markov model, the variance of the bias state stays bounded, even during time intervals when the bias state is not observable (see eqn. (4.102) in [3]). However, when the bias is unobservable, the bias state estimate itself tends to zero during time-propagation (i.e., the previously estimated quantity is slowly forgotten). Whether this is relevant or not depends on the duration of time without observability of the bias state and Gauss-Markov model correlation time.

With the Gauss-Markov choice, eqn. (20) reduces to:

$$\vec{z}_a = \vec{z}_N + \vec{z}_G.$$

The augmented system model is given by

$$\begin{bmatrix} \dot{\vec{v}}_{eb}^n \\ \dot{\vec{z}}_G \end{bmatrix} = \begin{bmatrix} \mathbf{C}_b^n \tilde{\vec{f}}_{ib}^b - (2\vec{\omega}_{ie}^n + \vec{\omega}_{en}^n) \times \vec{v}_{eb}^n + \vec{g}_l^n - \mathbf{C}_b^n \vec{z}_G \\ -\vec{\mu}_B \vec{z}_G \end{bmatrix} + \begin{bmatrix} -\mathbf{C}_b^n \\ \mathbf{I} \end{bmatrix} \begin{bmatrix} \vec{\omega}_N \\ \vec{\omega}_B \end{bmatrix}, \quad (74)$$

with the velocity random walk (i.e., $\vec{\omega}_N$) and the driving noise of the Gauss-Markov model (i.e., $\vec{\omega}_B$) constituting the process noise.

This state augmentation allows for a calibration of the inertial sensors during the mission, which improves the inertial navigation performance, especially when no aiding information is available. The time-correlated nature of the inertial sensor biases is respected, and the sensor characteristics represented in the corresponding ASD plot are modeled to the extent (i.e., cluster duration) where they are meaningful for the application. For example, typically in a GNSS/INS system, GNSS measurements are processed with a rate of approximately 1 Hz. This means that the time interval over which the INS propagates the state, without

aiding corrections, is normally limited to 1 second. Using inertial sensors up to tactical grade, an inertial-only navigation during GNSS outages is only meaningful for a few minutes at best, because the inertial navigation errors grow with time relatively quickly. In consequence, from the point of view of the filter design, it is not required to model inertial sensor characteristics that become dominant in the ASD plot for time intervals of several hundreds or thousands of seconds.

While the advantages of such an augmentation have just been outlined, as discussed earlier, the augmentation with additional states increases the computational load. Before augmentation with inertial sensor biases, a tightly coupled GNSS/INS filter would typically require eleven states: three position error states, three velocity error states, three attitude error states, and two states for the receiver clock error model. For multi-GNSS implementations, additional clock model states are required per constellation. The augmentation with accelerometer and gyroscope bias states (either \bar{z}_G or \bar{z}_K) adds six states, which increases the computational load by roughly a factor of four. Augmentation with two states per instrument (e.g., both \bar{z}_G and \bar{z}_K) adds twelve states, which increases the computational load by roughly a factor of ten.

F. Deterministic Errors

So far, for stochastic error modeling, only the ASD plots provided by the sensor manufacturer have been considered. However, when designing a sensor fusion filter, additional ‘deterministic’ aspects of the IMU may need to be addressed. Inertial sensor manufacturers usually provide a variety of specifications in addition to the ASD plots, which are addressed briefly below.

Misalignment. The IMU axis-to-axis misalignment describes the non-orthogonality of the sensitive axes of the sensors. Some manufacturers provide a typical standard deviation for the angle by which two sensor axes may deviate from an ideal ninety degrees. With sufficient dynamics and inertial sensor accuracy, misalignment could be estimated in the navigation filter, adding nine states defined as follows. The IMU sensitive axes span the body frame. When considering misalignment, it has to be defined how this is to be understood. One possible approach is to define the sensitive axis of the z -accelerometer as z -axis of the body frame. The non-orthogonality of the y -accelerometer axis to the z -accelerometer axis can be described with a single angle. The x -axis is defined as the unique vector that is orthogonal to the y - z plane, so that the body frame is defined completely. The description of the misalignment of x -accelerometer, and x , y , and z -gyroscopes with respect to this body frame, require two angles for each sensor, adding up to nine states total. An IMU axis to platform frame misalignment, which is to be understood as a simple rotation of the body frame with respect to the IMU frame that it is supposed to be aligned with, has no negative impact on inertial navigation performance.

Nonlinearity. This term refers to the deviation of the sensor input-output curve from a straight line. A line is fit to the input-output curve and the maximum deviation of the input-output curve with respect to this fitted line, divided by the sensor measurement range (full scale), is defined as non-linearity. The nonlinearity usually cannot be estimated in the navigation filter.

Scale Factor. In the definition of nonlinearity, the line would ideally have a slope of one. The deviation of the actual slope

from one is the scale factor error (often stated in parts per million). Scale factor error could potentially be estimated in the navigation filter, adding six states, three for the gyroscopes and three for the accelerometers. However, as for the misalignment, the linear scale factor error is often difficult to observe. Without vehicle motion both scale factor and misalignment are indistinguishable from biases.

Linear acceleration effect. MEMS gyroscopes show an acceleration-dependent bias error. Usually, a navigation filter does not consider this type of error explicitly.

Vibration rectification error. This is especially relevant to accelerometers that exhibit a vibration dependent bias. Possible reasons for such a vibration dependent bias include nonlinearity and aliasing. Usually, a navigation filter does not consider this type of error explicitly.

The above brief discussion of deterministic sensor errors states that some of them (e.g., nonlinearity) cannot be accounted for explicitly in the Kalman filter system model. Whether the augmentation of states for scale factor and misalignment calibration is worthwhile is application dependent. First, not all of them are observable individually. Second, the increase in computational complexity could be prohibitive. Furthermore, the IMU is often exposed to vibrations. Vibrations are micro-movements of the sensor, which may not be resolved correctly by the IMU and INS strapdown algorithm. For example, the frequency of some of the vibrations may exceed the Nyquist frequency of the sensor, causing aliasing to occur. These errors might be modeled as additional time-correlated noise, however as this requires at least second order Gauss-Markov models, such a solution would require twelve additional states. Instead of explicitly considering vibration induced noise, misalignment, linear and non-linear scale factor errors, an often used approach is to increase the navigation filter process noise beyond the levels that have been obtained from an analysis of the ASD plot.

G. IMU Manufacturer Terminology

This section briefly discusses various additional terms that appear on some manufacturer data sheets.

Bias in-run stability. The bias in-run stability is the component of the total sensor bias that varies with time in a correlated fashion. This correlated temporal variation is typically modeled as a first-order Gauss-Markov process, i.e., $z_G(k)$. The bias in-run stability (or in-run bias) is described on IMU data sheets with units that correspond to the ASD. In accordance with the IEEE specifications [28], [30], this value corresponds to B at the minimum of the ASD plot, as discussed relative to eqn. (32). However, the cluster time corresponding to this minimum value is typically not provided by sensor manufacturers, but can be extracted from the ASD plot, if provided; otherwise, the correlation time must be selected and tuned by the designer.

Turn-on bias. The turn-on bias (also referred to as the start-up, run-to-run, or repeatability bias) is an offset in the sensor readings, that potentially changes each time the sensor is switched on. The total inertial sensor bias can be seen as the sum of this turn-on bias and a time varying contribution (i.e., bias in-run stability). The turn-on bias is relevant for the initialization of the variance of the inertial sensor bias states in the navigation filter. Using the

state vector defined relative to eqn. (48) as an example, the initial covariance of the augmented states $z_G(0)$ and $z_K(0)$ should be selected to add up to the manufacturer specified variance of the turn-on bias. As explained in the “Observability: Where is the Bias?” section, the turn-on bias cannot be inferred from an ASD plot.

Angle/velocity random walk. The random walk describes the impact of the sensor inherent white noise when integrating. The unit is $\frac{\circ}{\sqrt{h}}$ for gyroscopes and $\frac{m/s}{\sqrt{h}}$ for accelerometers. An angular random walk of $\alpha \frac{\circ}{\sqrt{h}}$ indicates that after integrating angular rate measurements for H hours, an angle error standard deviation of $\alpha \sqrt{H}$ degrees will result due to the sensor inherent white noise. The random walk contributes to the process noise in the navigation filter system model (e.g., see eqn. (74)). The angle/velocity random walk parameter is the square root of the power spectral density of the sensor inherent white noise, which is denoted by N throughout this paper. In some data sheets, the angle/velocity random walk is referred to as the *noise density*, typically provided with the unit $\frac{\circ/h}{\sqrt{Hz}}$ for gyroscopes and $\frac{m/s^2}{\sqrt{Hz}}$ for accelerometers. The noise density is an alternative representation to the random walk parameter N . It is possible to convert between both representations of the sensor inherent white noise. For example,

$$\frac{m/s^2}{\sqrt{Hz}} = \frac{m \sqrt{s}}{s^2} = \frac{m/s}{\sqrt{s}} = 60 \frac{m/s}{\sqrt{h}}.$$

VIII. AVAILABLE SOFTWARE PACKAGE

An open-source Matlab software package is available at <https://github.com/jaffarrell/AV-Matlab-SW>. The software has two components. The first component completes the following: (1) Given a continuous-time error model, it computes an equivalent discrete-time state-space model. (2) Given that discrete-time model, a simulation produces a stochastic error sequence $z_k = z(t_k)$ where $t_k = kT$ for $k = 1, \dots, L$. (3) Given a sequence of stochastic errors $\{z_k\}_{k=1}^L$, it computes the Allan Variance (i.e., $\sigma_u^2(\tau)$) and plots the Allan Standard Deviation (i.e., $\sqrt{\sigma_u^2(\tau)}$). The second component implements the optimization-based approach described in eqns. (63-64) to fit the parameters of the NBK continuous-time state-space model described in eqns. (40-42) to a given set of AV data. Together, these two components enable a complete design cycle. Inclusion of the optimization-based approach is for completeness, it is not meant to imply that it is the recommended approach for selecting the state-space stochastic error model.

This software release includes a dataset for the demonstration example herein. The user must adapt that approach and software to the model appropriate for their instrument.

IX. CONCLUSIONS

The main purpose of this article has been to present a tutorial on the process that starts from an instrument’s ASD plot (or its derived parameters) and constructs a state-space IMU error model suitable for real-time INS error state estimation and IMU calibration using data fusion methods such as the KF, EKF, UKF, PF, or MAP. An example model construction and verification method is included. We do not claim that this approach is unique or optimal. It is representative of industry-standard methods.

In addition, as a tutorial, we have included an extensive discussion of the issues and trade-offs that a designer should consider, including: performance, computational load, observability, and extent of the cluster time τ that is relevant to a given application.

Finally, the manufacturer provided ASD plot or parameters should be considered as a starting point. It will dictate the dominant forms of error and reasonable values for the error model parameters. Minor tuning relative to those reasonable parameters will normally be required to accommodate: the particular IMU that is available; and, error terms that were ignored or neglected due to observability or computational reasons. A considerable tuning might be required, in case the IMU is exposed to vibrations containing frequencies exceeding the Nyquist frequency.

X. ACKNOWLEDGMENTS

The authors greatly appreciate the efforts of the anonymous reviewers and editorial team. Their comments enhanced the presentation and readability of the article. Specifically, the model robustness ideas of the penultimate sentence in the penultimate paragraph of the “Bias Instability: $z_B(t)$ ” section and in the last sentence in the “Computational Impact of Augmented States” section are based on suggestions from the reviewers.

The authors also thank Zhiqiang Xing and Demoz Gebre-Egziabher for supplying the IMU data and answering questions that helped to create Fig. 1; and Y. Yang of Nav Technology for supplying the IMU data that is the basis of Figs. 2, 8, and 9.

The optimization-based approach is not original to this article. It is practiced in industry. The general idea was explained to the first author by John R. Dowdle and Karl W. Flueckiger in the early 1990’s.

This work was supported in part by the Coordination for the Improvement of Higher Education Personnel (CAPES), under grant 88881.169927/2018-01; the Brazilian Agricultural Research Corporation (EMBRAPA), under grant 212-20/2018; and, the Brazilian National Council for Scientific and Technological Development (CNPq), under grant 313160/2019-8.

REFERENCES

- [1] K. R. Britting, *Inertial Navigation Systems Analysis*. John Wiley & Sons Canada, Limited, 1971.
- [2] M. M. Kuritsky and M. S. Goldstein, “Inertial navigation,” *Proc. of the IEEE*, vol. 71, no. 10, p. 1156–1176, 1983.
- [3] J. A. Farrell, *Aided Navigation: GPS with High Rate Sensors*. McGraw-Hill, Inc., 2008.
- [4] P. D. Groves, *Principles of GNSS, Inertial, and Multisensor Integrated Navigation Systems*. London: Artech House Remote Sensing Library, 2013.
- [5] M. S. Grewal, A. P. Andrews, and C. G. Bartone, *Global Navigation Satellite Systems, Inertial Navigation & Integration*. John Wiley & Sons, 2013.
- [6] D. A. Grejner-Brzezinska, C. K. Toth, T. Moore, J. F. Raquet, M. M. Miller, and A. Kealy, “Multisensor navigation systems: A remedy for GNSS vulnerabilities?” *Proc. of the IEEE*, vol. 104, no. 6, p. 1339–1353, 2016.
- [7] R. E. Kalman, “A new approach to linear filtering and prediction problems,” *J. Basic Eng. - Trans. ASME*, vol. 82, no. D, pp. 35–45, 1960.
- [8] R. E. Kalman and R. S. Bucy, “New results in linear filtering and prediction theory,” *J. Basic Eng. - Trans. ASME*, vol. 1, pp. 95–108, 1961.
- [9] A. Gelb, J. F. Kasper Jr, R. A. Nash Jr, C. F. Price, and A. A. Sutherland Jr, *Applied Optimal Estimation*. Cambridge: Analytic Sciences Cooperation, 1974.
- [10] F. M. Mirzaei and S. I. Roumeliotis, “A Kalman filter-based algorithm for IMU-camera calibration: Observability analysis and performance evaluation,” *IEEE Trans. Robot.*, vol. 24, no. 5, pp. 1143–1156, 2008.

- [11] R. G. Brown and P. Y. C. Hwang, *Introduction to Random Signals and Applied Kalman Filtering with Matlab Exercises*, 2nd ed. Wiley, 1992.
- [12] J. A. Farrell, T. Givargis, and M. J. Barth, "Real-time differential carrier phase GPS-aided INS," *IEEE Transactions on Control Systems Technology*, vol. 8, no. 4, pp. 709–721, 2000.
- [13] A. I. Mourikis and S. I. Roumeliotis, "A Multi-State Constraint Kalman Filter for Vision-aided Inertial Navigation," *IEEE Int. Conf. Robotics and Automation*, 2007.
- [14] J. Civera, A. J. Davidson, and J. M. Montiel, "Inverse depth parametrization for monocular SLAM," *IEEE T. Robotics*, vol. 24, no. 5, pp. 932–945, 2008.
- [15] M. Li, B. H. Kim, and A. I. Mourikis, "Real-time motion tracking on a cellphone using inertial sensing and a rolling-shutter camera," *IEEE Int. Conf. Robotics and Automation*, 2013.
- [16] S. Julier, J. Uhlmann, and H. Durrant-Whyte, "A new method for the non-linear transformation of means and covariances in filters and estimators," *IEEE T. Autom. Control*, vol. 45, no. 3, p. pages, 477–482.
- [17] S. Julier and J. Uhlmann, "Unscented filtering and nonlinear estimation," *Proc. of the IEEE*, vol. 92, no. 3, p. 401–422, 2004.
- [18] J. L. Crassidis, "Sigma-point Kalman filtering for integrated GPS and inertial navigation," *IEEE T. Aerospace and Electronic Systems*, vol. 42, no. 2, pp. 750–756, 2006.
- [19] J. S. Liu and R. Chen, "Sequential Monte Carlo methods for dynamic systems," *J. of the American Stat. Assoc.*, vol. 93, no. 443, pp. 1032–1044, 1998.
- [20] M. Pitt and N. Shephard, "Filtering via simulation: auxiliary particle filter," *J. of the American Stat. Assoc.*, vol. 94, pp. 590–599, 1999.
- [21] A. Doucet, J. de Freitas, and N. Gordon, Eds., *Sequential Monte Carlo Methods In Practice*. Springer-Verlag, 2001.
- [22] S. Thrun, W. Burgard, and D. Fox, "A probabilistic approach to concurrent mapping and localization for mobile robots," *Mach. Learn.*, vol. 31, no. 1-3, pp. 29–53, 1998. [Online]. Available: <http://dx.doi.org/10.1023/A:1007436523611>
- [23] F. Dellaert and M. Kaess, "Square Root SAM: Simultaneous localization and mapping via square root information smoothing," *Intl. J. of Robotics Research, IJRR*, vol. 25, no. 12, pp. 1181–1204, Dec 2006.
- [24] R. Eustice, H. Singh, J. J. Leonard, M. Walter, and R. Ballard, "Visually navigating the RMS Titanic with SLAM information filters," *Robotics: Science and Systems*, 2005.
- [25] R. Eustice, H. Singh, and J. J. Leonard, "Exactly sparse delayed-state filters for view-based SLAM," *IEEE T-Rob.*, vol. 22, p. 1100 – 1114, 2006.
- [26] M. Kaess, A. Ranganathan, and F. Dellaert, "iSAM: Incremental Smoothing and Mapping," *IEEE T-Rob.*, vol. 24, no. 6, p. 1365 – 1378, 2008.
- [27] S. Zhao, Y. Chen, H. Zhang, and J. A. Farrell, "Differential GPS aided inertial navigation: A contemplative realtime approach," *IFAC*, pp. 8959–8964, 2014.
- [28] IEEE, "Specification Format Guide and Test Procedure for Single-Axis Interferometric Fiber Optic Gyros," *Standard 952*, R2003.
- [29] —, "Specification Format Guide and Test Procedure for Linear, Single-Axis, Non-Gyroscopic Accelerometers," *Standard 1293*, 1999.
- [30] —, "Specification Format Guide and Test Procedure for Single-Axis Laser Gyros," *Standard 647*, R2006.
- [31] J. Baziw and C. T. Leondes, "In-flight alignment and calibration of inertial measurement units - Part I: General formulation," *IEEE Trans. Aero. Elec. Sys.*, vol. 8, no. 4, pp. 439–449, 1972.
- [32] A. J. Dierendonck, J. B. McGraw, and R. G. Brown, "Relationship between Allan variances and Kalman filter parameters," in *Proc. 16th Annual Precise Time and Time Interval (PTTI) Applications and Planning Meeting*. Greenbelt, MD: NASA Goddard Space Flight Center, 1984, pp. 273–293.
- [33] J. J. Ford and M. E. Evans, "Online estimation of Allan variance parameters," *Journal of Guidance, Control, and Dynamics*, vol. 23, no. 6, pp. 980–987, 2000.
- [34] N. El-Sheimy, H. Hou, and X. Niu, "Analysis and modeling of inertial sensors using Allan variance," *IEEE T. on Instrumentation and Measurement*, vol. 57, no. 1, pp. 140–149, 2008.
- [35] X. Zhang, Y. Li, P. Mumford, and C. Rizos, "Allan variance analysis on error characters of mems inertial sensors for an FPGA-based GPS/INS system," *International Symposium on GPS/GNSS*, p. 127–133, 2008.
- [36] Z. Xing and D. Gebre-Egziabher, "Modeling and bounding low cost inertial sensor errors," in *Proc. Position Location and Navigation Symp.* Monterey: IEEE, 2008, pp. 1122–1132.
- [37] V. Saini, S. C. Rana, and M. M. Kube, "Online estimation of state space error model for MEMS IMU," *Journal of Modelling & Simulation of Systems*, vol. 1, no. 4, pp. 219–225, 2010.
- [38] V. Vaccaro and A. Zaki, "Statistical modeling of rate gyros," *IEEE T. Instrumentation and Measurement*, vol. 61, no. 3, pp. 673 – 684, 2012.
- [39] J. Hidalgo-Carri6, S. Arnold, and P. Poulakis, "On the design of attitude-heading reference systems using the Allan variance," *IEEE T. Ultrason., Ferroelectr., Freq. Control*, vol. 63, no. 4, pp. 656–665, 2016.
- [40] F. O. Silva, E. M. Hemerly, and W. C. Leite Filho, "On the error state selection for stationary SINS alignment and calibration Kalman filters - Part II: Observability/estimability analysis," *Sensors*, vol. 17, no. 439, pp. 1–34, 2017.
- [41] D. H. Titterton and J. L. Weston, *Strapdown Inertial Navigation Technology*. Reston: Institution of Electrical Engineers, 2004.
- [42] R. Zhang, F. Hoflinger, and L. M. Reindl, "Calibration of an IMU using 3-D rotation platform," *IEEE Sens. J.*, vol. 14, no. 6, pp. 1778–1787, 2014.
- [43] Y. Stebler, S. Guerrier, J. Skaloud, and M. P. Victoria-Feser, "A framework for inertial sensor calibration using complex stochastic error models," in *Proc. Position, Location and Navigation Symp.* Myrtle Beach: IEEE, 2012, pp. 849–861.
- [44] A. G. Quinchia, G. Falco, E. Falletti, F. Dovis, and C. Ferrer, "A comparison between different error modeling of MEMS applied to GPS/INS integrated systems," *Sensors*, vol. 13, no. 1, pp. 9549–9588, 2013.
- [45] Crossbow, "Specification sheet for the μ nav navigation & servo control board," *Document No. 6020-0083-02, Rev. B.*, 2006.
- [46] S. Nassar, K. P. Scharzw, and N. El-Sheimy, "Modeling inertial sensor errors using autoregressive AR models," *Navigation*, vol. 51, no. 4, pp. 259–268, 2004.
- [47] Z. Miao, F. Shen, D. Xu, K. He, and C. Tian, "Online estimation of Allan variance coefficients based on a neural-extended Kalman filter," *Sensors*, vol. 15, no. 1, pp. 2496–2524, 2015.
- [48] W. J. Riley, *Handbook of Frequency Stability Analysis*, ser. Volume 1065 of NIST special publication. U.S. Department of Commerce, National Institute of Standards and Technology, 2008.
- [49] D. W. Allan, "Statistics of atomic frequency standards," *Proc. of the IEEE*, vol. 54, no. 2, pp. 221–230, 1966.
- [50] J. A. Barnes, A. R. Chi, L. S. Cutler, D. J. Healey, D. B. Leeson, T. E. McGunigal, J. A. Mullen Jr., W. L. Smith, R. L. Sydnor, R. F. C. Vessot, and G. R. Winkler, "Characterization of frequency stability," *IEEE Trans. Instrum. Meas.*, vol. IM-20, no. 2, pp. 105–120, 1971.
- [51] P. Lesage and C. Audoin, "Characterization of frequency stability: uncertainty due to the finite number of measurements," *IEEE Trans. Instrum. Meas.*, vol. 22, no. 5, pp. 157–161, 1973.
- [52] —, "Correction to "characterization of frequency stability: uncertainty due to the finite number of measurements"," *IEEE Trans. Instrum. Meas.*, vol. 25, no. 3, pp. 270–270, 1976.
- [53] M. M. Tehrani, "Ring laser gyro data analysis with cluster sampling technique," *Proc. SPIE*, vol. 412, no. 1, pp. 207–220, 1983.
- [54] J. Li and J. Fang, "Not fully overlapping Allan variance and total variance for inertial sensor stochastic error analysis," *IEEE Trans. Instrum. Meas.*, vol. 62, no. 10, pp. 2659–2672, 2013.
- [55] H. Hou, *Modeling Inertial Sensors Errors Using Allan Variance*. MS Thesis, University of Calgary, September 2004, no. UCGE 20201.
- [56] R. G. Brown and P. Y. C. Hwang, *Introduction to Random Signals and Applied Kalman Filtering with Matlab Exercises*. Wiley, 2012.
- [57] W. Gautschi and W. F. Cahill, *Exponential Integral and Related Functions: Handbook of Mathematical Functions with Formulas, Graphs, and Mathematical Tables*. New York: Dover, 1972.
- [58] P. G. Savage, *Strapdown Analytics*. Maple Plain: Strapdown Associates, 2007.
- [59] N. J. Kasdin, "Discrete simulation of colored noise and stochastic processes and $1/f^\alpha$ power law noise generation," *Proc. of the IEEE*, vol. 83, no. 5, pp. 802–827, 1995.
- [60] C. Van Loan, "Computing integrals involving the matrix exponential," *IEEE Transactions on Automatic Control*, vol. 23, no. 3, 1978.
- [61] W. Wrigley, "History of inertial navigation," *NAVIGATION: Journal of the Institute of Navigation*, vol. 24, no. 1, Spring 1977.
- [62] A. Lawrence, *Modern Inertial Technology*. Springer, 1993.
- [63] P. Teunissen and O. Montenbruck, Eds., *Springer Handbook of Global Navigation Satellite Systems*. Springer, 2017.
- [64] P. S. Maybeck, *Stochastic Models, Estimation and Control*. London: Academic Press, Inc., 1979.
- [65] F. M. Ham and R. G. Brown, "Observability, eigenvalues, and Kalman filtering," *IEEE Trans. Aero. Elec. Sys.*, vol. 19, no. 2, pp. 269–273, 1983.
- [66] J. E. Potter and R. G. Stern, "Statistical filtering of spacecraft navigation measurements," *Proc. AIAA Guidance and Control Conf.*, 1963.
- [67] G. H. Golub, "Numerical methods for solving least squares problems," *Numer. Math.*, vol. 7, pp. 206–216, 1965.
- [68] S. F. Schmidt, "Computational techniques in kalman filtering," *NATO-AGARD-139*, 1970.

- [69] —, “Sequential square root filtering and smoothing of discrete linear systems,” *Automatica*, vol. 10, pp. 147–158, 1974.
- [70] K. R. Britting, “Self-alignment techniques for strapdown inertial navigation systems with aircraft application,” *J. Aircraft*, vol. 7, no. 4, pp. 302–307, 1970.
- [71] V. Krishnan and K. Grobert, “Initial alignment of a gimballess inertial navigation system,” *IEEE Trans. Automat. Contr.*, vol. 15, no. 6, pp. 667–671, 1970.
- [72] J. Baziw and C. T. Leondes, “In-flight alignment and calibration of inertial measurement units - part II: Experimental results,” *IEEE Trans. Aero. Elec. Sys.*, vol. 8, no. 4, pp. 450–465, 1972.
- [73] I. Y. Bar-Itzhack and B. Porat, “Azimuth observability enhancement during inertial navigation system in-flight alignment,” *J. Guid. Control*, vol. 3, no. 4, pp. 337–344, 1980.
- [74] B. Porat and B.-I. I. Y., “Effect of acceleration switching during INS in-flight alignment,” *J. Guid. Control*, vol. 4, no. 4, pp. 385–389, 1981.
- [75] I. Y. Bar-Itzhack and N. Berman, “Control theoretic approach to inertial navigation systems,” *J. Guid. Control*, vol. 11, no. 3, pp. 237–245, 1988.
- [76] D. Goshen-Meskin and I. Y. Bar-Itzhack, “Observability studies of inertial navigation systems,” *J. Guid. Control*, vol. 11, no. 3, pp. 1283–1289, 1989.
- [77] S. Hong, M. H. Lee, H. H. Chun, S. H. Kwon, and J. L. Speyer, “Observability of error states in GPS/INS integration,” *IEEE Trans. Aero. Elec. Sys.*, vol. 54, no. 2, pp. 731–743, 2005.
- [78] I. Rhee, M. F. Abdel-Hafez, and J. L. Speyer, “Observability of an integrated GPS/INS during maneuvers,” *IEEE Trans. Aero. Elec. Sys.*, vol. 40, no. 2, pp. 1362–1366, 2004.
- [79] F. O. Silva, E. M. Hemerly, and W. C. Leite Filho, “Error analysis of analytical coarse alignment formulation for stationary SINS,” *IEEE Trans. Aero. Elec. Sys.*, vol. 52, no. 4, pp. 1777–1796, 2016.
- [80] F. O. Silva, E. M. Hemerly, W. C. Leite Filho, and H. K. Kuga, “A fast in-field coarse alignment and bias estimation method for stationary intermediate-grade IMUs,” *IEEE Trans. Instrum. Meas.*, vol. 67, no. 4, pp. 831–838, 2018.
- [81] A. E. Bryson, “Kalman filter divergence and aircraft motion estimators,” *J. Guidance and Control*, vol. 1, no. 1, pp. 71–79, 1978.
- [82] A. H. Jazwinski, “Limited memory optimal filtering,” *IEEE TAC*, vol. 13, no. 5, pp. 558–563, 1968.
- [83] J. H. L. K. R. Muske, J. B. Rawlings, “Receding horizon recursive state estimation,” *ACC*, pp. 900–904, 1993.
- [84] P. E. Moraal and J. W. Grizzle, “Observer design for nonlinear systems with discrete-time measurements,” *IEEE TAC*, vol. 40, no. 3, pp. 395–404, 1995.
- [85] W. Li, W. Li, X. Cui, S. Zhao, and M. Lu, “A tightly coupled rtk/ins algorithm with ambiguity resolution in the position domain for ground vehicles in harsh urban environments,” *Sensors*, vol. 18, no. 7, p. 2160, 2018.
- [86] E. Parzen, *Stochastic Processes*. San Francisco: Holden-Day, 1962.
- [87] D. W. Allan and J. A. Barnes, “A modified “Allan variance” with increased oscillator characterization ability,” in *Proc. 35th Annual Frequency control Symposium*. Fort Monmouth: USA ERADCON, 1981, pp. 471–475.
- [88] D. A. Howe, D. W. Allan, and J. A. Barnes, “Properties of signal sources and measurement methods,” in *Proc. 35th Annual Frequency control Symposium*. Fort Monmouth: USA ERADCON, 1981, pp. A1–A47.
- [89] J. Rutman, “Characterization of phase and frequency instabilities in precision frequency sources: fifteen years of progress,” *Proc. of the IEEE*, vol. 66, no. 9, pp. 1048–1075, 1978.
- [90] F. L. Walls and D. W. Allan, “Measurements of frequency stability,” *Proc. of the IEEE*, vol. 74, no. 1, pp. 162–168, 1986.
- [91] P. Lesage and C. Audoin, “Estimation of the two-sample variance with a limited number of data,” in *Proc. 31st Annual Symposium on Frequency Control*. Atlantic City: IEEE, 1977, pp. 311–318.
- [92] K. Yoshimura, “Characterization of frequency stability: uncertainty due to the autocorrelation of the frequency fluctuations,” *IEEE Trans. Instrum. Meas.*, vol. 27, no. 1, pp. 1–7, 1978.
- [93] P. Lesage and C. Audoin, “Characterization of measurement of time and frequency stability,” *Radio Science*, vol. 14, no. 4, pp. 521–539, 1979.
- [94] C. A. Greenhall, “A structure function representation theorem with applications to frequency stability estimation,” *IEEE Trans. Instrum. Meas.*, vol. 32, no. 2, pp. 364–370, 1983.
- [95] D. Yuan, X. Ma, Y. Liu, Z. Shang, and S. Yan, “Statistical modeling of random walk errors for triaxial rate gyros,” *IEEE Trans. Instrum. Meas.*, vol. 65, no. 2, pp. 286–296, 2016.
- [96] P. Lesage and C. Audoin, “Comments on “characterization of frequency stability: uncertainty due to the finite number of measurements,”” *IEEE Trans. Instrum. Meas.*, vol. 24, no. 1, pp. 86–86, 1975.
- [97] —, “Effect of dead-time on the estimation of the two-sample variance,” *IEEE Trans. Instrum. Meas.*, vol. 28, no. 1, pp. 6–10, 1979.
- [98] K. Yoshimura, “Degrees of freedom of the estimate of the two-sample variance in the continuous sampling method,” *IEEE Trans. Instrum. Meas.*, vol. 38, no. 6, pp. 1044–1049, 1989.
- [99] C. A. Greenhall, “Recipes for degrees of freedom of frequency stability estimators,” *IEEE Trans. Instrum. Meas.*, vol. 40, no. 6, pp. 994–999, 1991.
- [100] T. Walter, “Characterizing frequency stability: A continuous power-law model with discrete sampling,” *IEEE Trans. Instrum. Meas.*, vol. 43, no. 1, pp. 69–79, 1994.
- [101] P. Lesage and T. Ayi, “Characterization of frequency stability: Analysis of the modified Allan variance and properties of its estimate,” *IEEE Trans. Instrum. Meas.*, vol. 33, no. 4, pp. 332–336, 1984.
- [102] A. H. Jazwinski, *Stochastic Processes and Filtering Theory*, ser. Mathematics in Science and Engineering. New York: Academic Press, Inc., 1970.
- [103] R. E. Kalman, T. S. Englar, and R. S. Bucy, “Fundamental study of adaptive control systems,” *ASD-TR-61-27*, vol. 1, 1962.

A. Sidebar: Nontechnical Article Summary

Autonomous vehicles utilize control systems to cause the vehicle state to follow a desired trajectory. The control system incorporates information about the vehicle position, velocity, acceleration, attitude, and angular rate which can be computed by integration of the measurements of an inertial measurement unit (IMU). This integrative process also accumulates IMU measurement errors that cause the integrated IMU measurements, which is the vehicle state estimate, to slowly diverge from the true vehicle state. The difference is referred to as the vehicle error state vector. This vehicle error state vector and various IMU calibration parameters can be estimated through the state estimation process using information from external sensors (e.g., camera, GNSS, Lidar, Radar). Such real-time calibration of the IMU (and other sensors) results in improved accuracy and slower rates of IMU error accumulation during the time intervals between the measurements from external sensors.

Design of the state estimator requires definition of the IMU error state vector and its stochastic discrete-time state-space model. This modeling process begins from the IMU performance specification information provided by the IMU manufacturer, which per the IEEE standards is communicated through the Allan Variance. Information extracted from the Allan standard deviation graph allows the analyst to evaluate various issues and trade-offs involved in selecting the continuous-time IMU error state-space model. This tutorial article discusses this approach, the issues and trade-offs, the translation of the continuous-time model to an equivalent discrete-time model for implementation, and a verification approach. Example Matlab scripts are supplied that implement each step of this process.

B. Sidebar: Aided INS History

The first use of inertial navigation dates back to the German V-2 missile in 1942. After World War II, the United States started to develop inertial navigation systems (INS) for ballistic missiles, and later in the 1960’s also for the Apollo missions, as well as military and commercial airplanes [61]. The early inertial navigation systems used a gimballed platform that decoupled the host vehicle attitude changes from those of the platform. This decoupling allowed three accelerometers mounted on the platform to maintain alignment with the north, east, and down directions. For many applications, also a reduced set of sensors

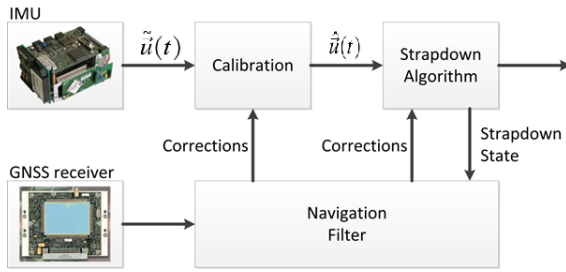


Fig. 10. Generic Block Diagram of a GNSS-aided INS.

was sufficient, e.g. the vertical axis and respective sensors were omitted. Because the initial position and velocity were known, integration of the accelerometer measurements propagated the position and velocity vectors forward in time. Gyroscopes were used to measure small perturbations of the platform attitude, which were then compensated mechanically to maintain the alignment of the accelerometers with the north, east and down directions.

These gimbaled systems, despite their impressive accuracy, had several drawbacks. The mechanical construction was complex, bulky, and expensive. Furthermore, aerobatic maneuvers could cause a gimbal lock: when two gimbal axes become aligned, a rotation perpendicular to this axis causes the platform to lose alignment. A solution was to add a fourth gimbal, which further increased complexity and cost [62].

Advances in electronic and gyroscope technology in the 1960's enabled the development of strapdown INS. In a strapdown INS, an inertial measurement unit (IMU) consisting of three accelerometers and three gyroscopes is attached rigidly to the host vehicle. The gyroscopes measure the attitude changes of the host vehicle, thereby enabling computational tracking of its attitude. This requires that these gyroscopes be capable of accurately measuring angular rates of up to several hundred degrees per seconds, for highly agile host platforms, whereas for a gimbaled system a gyroscope measurement range of few degrees per hour would have been sufficient. Knowledge of the host vehicle attitude allows transformation of the accelerometer measurements of the specific force from the body frame to an Earth reference frame (e.g. a north-east-down fixed tangent frame), in which compensation of gravity is straightforward; thereby yielding measurements of the host vehicle acceleration. As in a gimbaled system, this host vehicle acceleration is then integrated twice to compute the changing host vehicle position and velocity over time.

For any inertial navigation system (INS), gimbaled or strapdown, the errors in the inertial measurements accumulate, and together with the inaccuracies of the host vehicle initial state estimate, cause a deterioration of the accuracy of the navigation solution with time. To counter this temporal growth of position, velocity and attitude errors, the inertial navigation system can be corrected using aiding measurements from external sensors (e.g., GNSS receiver, camera, lidar, radar).

A typical GNSS-aided INS architecture is shown in Fig. 10. The strapdown algorithm numerically integrates the nonlinear kinematic model described in eqn. (2) using the calibrated IMU measurements $\hat{u}(t)$ as inputs. This integration is at the sampling rate of the IMU (e.g., 100's or 1000's of times per second),

which is designed to be high relative to the bandwidth of both the IMU and the host vehicle. When aiding sensor measurements are available, the navigation filter – often an extended or linearized Kalman filter – estimates corrections for the state and calibration factors. Aiding measurements are typically available at low rates (e.g., one vector measurement per second), relative to the host vehicle bandwidth. Calibration factors may include deterministic errors (e.g., scale factor and sensor-axis alignment errors) and time-correlated stochastic errors. This on-the-fly estimation of IMU calibration factors continuously re-calibrates the INS, leading to a superior INS performance during time intervals when aiding sensor measurements are not available (e.g., GNSS outages).

Two aided INS system architectures are widely used: loose and tight coupling, see Ch. 28 in [63]. In a *loosely coupled* GNSS-aided approach, the GNSS receiver computes position and velocity estimates internally from its pseudorange and Doppler measurements, without using INS information. This GNSS computation can occur only when the receiver has at least four satellites in view. When the GNSS position and velocity measurements are output from the receiver, the residual between them and their INS computed values are used to drive the navigation filter to estimate the INS error state; otherwise, the INS continues to integrate without correction. In a *tightly coupled* approach, the residual of the navigation filter is formed between the GNSS pseudorange and Doppler measurements and the predictions of those quantities as computed by the INS. This allows aiding even when fewer than four satellites are in view. The main trade-off is that tightly coupled systems offer the potential for higher-performance, especially when fewer measurements are available, but are more complex to implement due to the need for the navigation system: to process GNSS ephemeris data; to calculate satellite positions and velocities; and, to apply corrections for ionosphere, troposphere, satellite clocks and broadcast group delays. See Section 28.2 of [63]. Similar trade-offs apply for aiding with alternative aiding sensors.

There is a rich literature concerning dynamics, control, and system theoretic contributions within the inertial navigation context [1], [64]. Throughout their history, the Kalman filter has played an important role [7], [8], [65]. This history has included a focused effort on numerical methods [66], [67], [68], [69]. Observability studies for both stationary and time-varying systems is critical both for initialization and on-the-fly calibration [31], [70], [71], [72], [73], [74], [75], [76], [77], [78], [79], [80]. Also, understanding the controllability of the state from the perspective of the driving noise was critical to removing issues of Kalman filter divergence [81]. More recently, but still with a long history [82], [83], [84], efficient numeric methods for real-time trajectory (as opposed to state) estimation (i.e., real-time smoothing) are important for inertial-based simultaneous location and mapping applications [23], [24], [25], [26].

The ongoing decreases in the cost of inertial sensors, aiding measurements, and computation are allowing aided strapdown INS to be feasible with respect to both cost and accuracy in commercial applications. For example, the interest in combining GNSS-aided INS with Real Time Kinematic (RTK) techniques (See Chapter 26 in [63]) capable of achieving sub-meter accuracy

is growing. An overview on possible architectures is given in [85]. The performance of aided inertial systems is dependent on the navigation filter incorporating a state-space model of the IMU stochastic errors. This article provides a tutorial describing the industry standard process and trade-offs related to defining such models.

C. Sidebar: Simplified INS Example

This section presents a simplified two-dimensional INS example. The purpose is to present an example nonlinear kinematic model, show the INS equations that would propagate the vehicle state through time, show the linearized model that predicts the growth in the INS error over time, show how that error model is used to propagate the error covariance through time, and exemplify state augmentation for sensor calibration.

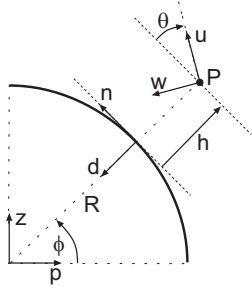


Fig. 11. Variables for 2-dimensional simplified INS example.

Various reference frames and variables are illustrated in Fig. 11. The Earth is assumed to be circular with radius R , non-rotating, and uniform density. The point P represents the location of the IMU on the vehicle. The vehicle is free to translate in \mathbb{R}^2 and rotate with one degree of freedom denoted by θ . The IMU sensitive axes are in the directions indicated by the unit vectors \tilde{u} and \tilde{w} , which define the vehicle reference frame. The origin of the geographic reference frame is defined as the projection of the point P onto the Earth surface, along the vector to the Earth's center. The instantaneous Earth tangent plane at the origin of the geographic frame defines the unit vectors \tilde{n} and \tilde{d} . The height of the point P above the tangent plane is the altitude h . The latitude ϕ and pitch θ are defined as positive in the directions indicated in the figure. The vectors \tilde{z} and \tilde{p} define the axes of the Earth centered reference frame.

The kinematic model for the IMU at point P (i.e., the vehicle model) is

$$\begin{bmatrix} \dot{\phi} \\ \dot{h} \end{bmatrix} = \begin{bmatrix} \frac{1}{R+h} & 0 \\ 0 & -1 \end{bmatrix} \begin{bmatrix} v_n \\ v_d \end{bmatrix} \quad (75)$$

$$\begin{bmatrix} \dot{v}_n \\ \dot{v}_d \end{bmatrix} = \tilde{a}_{iv}^g + \begin{bmatrix} \frac{v_n v_d}{R+h} \\ \frac{-v_n^2}{R+h} \end{bmatrix} \quad (76)$$

$$\dot{\theta} = \omega_{gv} \quad (77)$$

where \tilde{a}_{iv}^g is the inertially-referenced vehicle acceleration vector represented in geographic frame and ω_{gv} is the rotation rate of the vehicle relative to the geographic frame. This angular rate is computed as $\omega_{gv} = \omega_{iv} - \omega_{ig}$, where ω_{iv} is the rotation rate of the vehicle with respect to an inertial frame which is measured by the gyro and $\omega_{ig} = -\dot{\phi} = -\frac{v_n}{R+h}$ is the transport

rate of the geographic frame with respect to the inertial frame. The superscript g (or v) on the vector quantities indicates that the vector is represented in geographic (or vehicle) frame. The vector $[v_n, v_d]^T$ is the Earth relative velocity of point P represented in the instantaneous tangent plane. The second term on the right side of eqn. (76) is due to the rotation rate of the geographic frame with respect to the earth centered inertial frame (i.e., transport rate). Eqns. (75-77) are an example of the nonlinear kinematic model of eqn. (1) in the main body of this article.

For INS computations, the acceleration vector and angular rate are computed from the IMU measurements. The IMU consists of a dual-axis accelerometer and a single-axis gyro with output measurements modeled as

$$\tilde{u}_1^v = (\tilde{a}_{iv}^v - \tilde{g}^v) - \tilde{\varepsilon}_1^v = \tilde{f}^v - \tilde{\varepsilon}_1^v \quad (78)$$

$$\tilde{u}_2 = \omega_{iv} - \varepsilon_2 \quad (79)$$

where the tilde indicates a measurement, $\tilde{f} = \tilde{a}_{iv} - \tilde{g}$ is the specific force vector, and \tilde{g} represents the gravity vector. The terms

$$\tilde{\varepsilon}_1^v = -d_1^v(\tilde{u}) - z_1^v \text{ and } \varepsilon_2 = -d_2(\tilde{u}) - z_2$$

represent the sum of the deterministic and stochastic accelerometer and gyro errors, as defined in eqn. (3).

The IMU provides the measurements in v -frame, but they are needed for computations in g -frame. Vectors are transformed between frames using a direction cosine matrix, e.g., $\tilde{f}^g = R_v^g \tilde{f}^v$, where \tilde{f}^g is the specific force vector represented in geographic frame. The rotation matrix R_v^g from platform to geographic frame is defined as

$$R_v^g = \begin{bmatrix} \cos(\theta) & \sin(\theta) \\ -\sin(\theta) & \cos(\theta) \end{bmatrix}$$

and $R_v^v = (R_v^g)^T$.

A navigation system calculates the vehicle state by integration of the following equations

$$\begin{bmatrix} \hat{\phi} \\ \hat{h} \end{bmatrix} = \begin{bmatrix} \frac{1}{R+h} & 0 \\ 0 & -1 \end{bmatrix} \begin{bmatrix} \hat{v}_n \\ \hat{v}_d \end{bmatrix} \quad (80)$$

$$\begin{bmatrix} \hat{\dot{v}}_n \\ \hat{\dot{v}}_d \end{bmatrix} = \hat{R}_v^g (\tilde{u}_1^v + \hat{\varepsilon}_1^v) + \hat{g}^g(\hat{h}) + \begin{bmatrix} \frac{\hat{v}_n \hat{v}_d}{R+h} \\ \frac{-\hat{v}_n^2}{R+h} \end{bmatrix} \quad (81)$$

$$\hat{\dot{\theta}} = \frac{\hat{v}_n}{R+h} + (\tilde{u}_2 + \hat{\varepsilon}_2) \quad (82)$$

where $\hat{\varepsilon}_1$ is an estimate of the accelerometer error vector and $\hat{\varepsilon}_2$ is an estimate of the gyro error. Eqns. (80-82) provide an example of eqn. (2) in the main body of the article. The INS integrates these nonlinear equations to propagate the vehicle state through time.

The inputs to eqns. (1) and (2) are, respectively,

$$\tilde{u} = [(\tilde{u}_1^v)^T, u_2]^T \text{ and } \hat{\tilde{u}} = [(\hat{\tilde{u}}_1^v)^T, \hat{u}_2]^T.$$

Because the actual inputs $\tilde{u}_1^v = \tilde{a}_{iv}^v - \tilde{g}^v$ and $u_2 = \omega_{iv}$ are not available, for the purpose of integrating eqns. (80-82), they are computed from the measurements as

$$\hat{\tilde{u}}_1^v = \tilde{u}_1^v + \hat{\varepsilon}_1^v \text{ and } \hat{u}_2 = \tilde{u}_2 + \hat{\varepsilon}_2.$$

For use later, define

$$\begin{bmatrix} \hat{f}_n \\ \hat{f}_d \end{bmatrix} = \hat{R}_v^g \hat{u}_1^v. \quad (83)$$

The calibration terms $\hat{\varepsilon}_1^v$ and $\hat{\varepsilon}_2$ are computed using IMU error model parameters that are estimated in real-time. These calibration parameters are denoted as $\vec{x}_d(t)$ for the IMU deterministic errors and $\vec{x}_z(t)$ for the IMU stochastic errors in the augmented state vector defined in eqn. (5).

In this example, the vehicle state and estimated vehicle state are defined as

$$\vec{x}_v = [\phi, h, v_n, v_d, \theta]^\top \text{ and } \hat{\vec{x}}_v = [\hat{\phi}, \hat{h}, \hat{v}_n, \hat{v}_d, \hat{\theta}]^\top.$$

Because the actual state \vec{x}_v is not known, the navigation error state defined as $\delta\vec{x} = \vec{x}_v - \hat{\vec{x}}_v$ is also not known. Defining $\delta\vec{u} = \vec{u} - \hat{\vec{u}}$, the linearized error model of eqn. (4) would have

$$G(t) = \begin{bmatrix} 0 & 0 & 0 \\ 0 & 0 & 0 \\ \cos(\hat{\theta}) & \sin(\hat{\theta}) & 0 \\ -\sin(\hat{\theta}) & \cos(\hat{\theta}) & 0 \\ 0 & 0 & 1 \end{bmatrix}, \text{ and}$$

$$F(t) = \begin{bmatrix} 0 & -\frac{\hat{v}_n}{(R+\hat{h})^2} & \frac{1}{R+\hat{h}} & 0 & 0 \\ 0 & 0 & 0 & -1 & 0 \\ 0 & -\frac{\hat{v}_n \hat{v}_d}{(R+\hat{h})^2} & \frac{\hat{v}_d}{R+\hat{h}} & \frac{\hat{v}_n}{R+\hat{h}} & \hat{f}_d \\ 0 & \left(\frac{\hat{v}_n^2}{(R+\hat{h})^2} + \frac{\partial \hat{g}^v(h)}{\partial h} \Big|_{h=\hat{h}} \right) & \frac{-2\hat{v}_n}{R+\hat{h}} & 0 & -\hat{f}_n \\ 0 & -\frac{\hat{v}_n}{(R+\hat{h})^2} & \frac{1}{R+\hat{h}} & 0 & 0 \end{bmatrix}.$$

The main purpose of this tutorial is to discuss the issues and methods related to defining the stochastic error state vector $\vec{x}_z(t)$ and its state-space model in the form of eqn. (6). When this is done, the F and G matrices defined above are used with state augmentation methods to define the complete error model.

The augmented state-space model communicates to the mathematics of the state estimation process both how the IMU calibration states \vec{x}_d and \vec{x}_z change dynamically with time and how they affect the vehicle state estimate \vec{x}_v . The explicit method by which this is done is by using eqn. (86) to propagate the error state covariance matrix through time. It is critical to note that the vehicle state vector is propagated through time using the nonlinear kinematic model of eqn. (2), the linearized model of eqn. (86) is only used to propagate the error covariance matrix.

For more extensions to this example, such as its use to decouple the horizontal and vertical error dynamics to explain the vertical channel instability and horizontal channel Schuler oscillation, see p. 105 in [3].

In actual three-dimensional applications, the attitude representation and its update become more complicated; nevertheless, the basic approach and issues remain the same.

D. Sidebar: State Augmentation

The estimation algorithm estimates the augmented error state as defined in eqn. (5). The dimension of this augmented state is $n_x = n_v + n_d + n_z$.

The state-space error model for the vehicle error state is defined in eqn. (4). The state-space model for the IMU stochastic errors is defined in eqns. (6-7). For this sidebar, to allow for modeling three accelerometers and three gyros, the dimension of the output matrix will change to $C_z \in \mathbb{R}^{6 \times n_z}$.

Similarly, define the state-space model for the IMU deterministic errors as

$$\dot{\vec{x}}_d(t) = A_d \vec{x}_d(t) + B_d \vec{\omega}_d(t), \quad (84)$$

$$z_d(t) = C_d \vec{x}_d(t) \quad (85)$$

where $A_d \in \mathbb{R}^{n_d \times n_d}$, $B_d \in \mathbb{R}^{n_d \times r}$ and $C_d \in \mathbb{R}^{6 \times n_d}$. The parameter r represents the number of distinct noise processes in the deterministic error model. The parameter n_d represents the number of states selected to model the IMU deterministic errors. The elements of \vec{x}_d in the deterministic error model are usually considered to be unknown constants; therefore, the corresponding model has A_d , B_d , and r all being identically zero (i.e., $\vec{x}_d(t) = 0$).

Combining eqns. (4), (6-7), and (84-85) the linearized state-space error model has the form

$$\dot{\vec{x}} = \begin{bmatrix} F & G C_d & G C_z \\ 0 & 0 & 0 \\ 0 & 0 & A_z \end{bmatrix} \begin{bmatrix} \delta\vec{x}_v \\ \vec{x}_d \\ \vec{x}_z \end{bmatrix} + \begin{bmatrix} G & 0 \\ 0 & 0 \\ 0 & B_z \end{bmatrix} \begin{bmatrix} \vec{\eta}_z \\ \vec{\omega}_z \end{bmatrix} \quad (86)$$

where the time-dependence of all quantities has been dropped from the notation.

Given a set of aiding measurements, the objective of the data fusion system is to estimate the augmented error state vector $x(t)$ that is defined in eqn. (5) in real-time. Success requires that the state vector be observable, which is a well-studied problem [76], [77], [78].

E. Sidebar: Power Spectral Density

For a stationary process, the correlation function $R(\tau) = E\langle x(t)x(t+\tau) \rangle$ and two-sided PSD are Fourier transform pairs related by

$$S(\omega) = \int_{-\infty}^{\infty} e^{-j\omega\tau} R(\tau) d\tau \quad (87)$$

$$R(\tau) = \frac{1}{2\pi} \int_{-\infty}^{\infty} e^{j\omega\tau} S(\omega) d\omega \quad (88)$$

Instrument error models include non-stationary stochastic processes such as random walk and integrated random walk. Non-stationary stochastic processes can be analyzed using average correlation functions and average power spectrum (see Section 2.7 in [11] or p. 109 in [86]), which are related to each other in the same way as shown in eqns. (87-88). This article will not distinguish between the two.

F. Sidebar: Finite Dimensional Linear State-Space Systems have Even Power Spectra

The main text has stated that the power spectrum for a linear state-space model (without pure delay) will be an even polynomial function of $s = j\omega$. This sidebar discusses two aspects of this statement.

1) *State-Space to Transfer Function*: Consider the single-input single-output, finite dimensional, linear state-space model

$$\dot{\vec{x}}(t) = F \vec{x}(t) + G u(t), \quad (89)$$

$$z(t) = H \vec{x}(t) \quad (90)$$

where $F \in \mathbb{R}^{n \times n}$, $G \in \mathbb{R}^{n \times 1}$ and $H \in \mathbb{R}^{1 \times n}$. The parameter n represents the order of the system. The transfer function from u to z will be denoted by $\frac{Z(s)}{U(s)} = T(s)$, where s is the Laplace variable, $Z(s)$ and $U(s)$ are the Laplace Transforms of $z(t)$ and $u(t)$, respectively, and $T(s)$ can be computed from the state-space model parameters as (see Section 3.5.2: in [3]):

$$T(s) = H(sI - F)^{-1}G. \quad (91)$$

This transfer function is the ratio of polynomials in s , namely:

$$T(s) = \frac{N(s)}{D(s)}.$$

The purpose of this sidebar is to provide examples to demonstrate that the power spectrum

$$S(\omega) = T(s)T(s^*)|_{s=j\omega} = \frac{N(s)N(s^*)}{D(s)D(s^*)}|_{s=j\omega}$$

is an even polynomial function of ω .

Consider the double integrator state-space system:

$$\begin{aligned} \begin{bmatrix} \dot{p}(t) \\ \dot{v}(t) \end{bmatrix} &= \begin{bmatrix} 0 & 1 \\ 0 & 0 \end{bmatrix} \begin{bmatrix} p(t) \\ v(t) \end{bmatrix} + \begin{bmatrix} 0 \\ 1 \end{bmatrix} u(t) \\ z(t) &= \begin{bmatrix} 1 & 0 \end{bmatrix} \begin{bmatrix} p(t) \\ v(t) \end{bmatrix}. \end{aligned}$$

Using eqn. (91), the transfer function is

$$\frac{Z(s)}{U(s)} = \begin{bmatrix} 1 & 0 \end{bmatrix} \begin{bmatrix} s & -1 \\ 0 & s \end{bmatrix}^{-1} \begin{bmatrix} 0 \\ 1 \end{bmatrix} = \frac{1}{s^2}.$$

For $T(s) = \frac{1}{s^2}$,

$$S(\omega) = \frac{1}{(j\omega)^2} \frac{1}{(-j\omega)^2} = \frac{1}{\omega^4}$$

which is an even polynomial function of ω . Additional examples can be found in many text books. See for example Sections 3.2-3.7 in [56].

2) *Power Spectrum to State-Space*: The fact that any power spectrum $S(\omega)$ that is an even (finite order) polynomial function of ω can be represented by a finite dimensional linear state-space system is shown by first factoring $S(\omega) = T(j\omega)T(-j\omega)$ where T is the ratio of finite dimensional polynomials in $j\omega$ and then finding a state-space representation for $T(s)$. See Sections 3.2-3.7 in [56].

For example, the power spectrum $S(\omega) = \frac{A^2}{\omega^4}$, can be factored as $S(\omega) = \frac{A}{(j\omega)^2} \frac{A}{(-j\omega)^2}$ where the first term provides the transfer $T(s) = \frac{A}{s^2}$. The transfer function $\frac{Z(s)}{U(s)} = \frac{A}{s^2}$ is equivalent to

$s^2 Z(s) = A U(s)$. Multiplication by s in the Laplace domain corresponds to differentiation in the time domain; therefore, $\ddot{z}(t) = A u(t)$ which has the state-space model:

$$\begin{aligned} \begin{bmatrix} \dot{p}(t) \\ \dot{v}(t) \end{bmatrix} &= \begin{bmatrix} 0 & 1 \\ 0 & 0 \end{bmatrix} \begin{bmatrix} p(t) \\ v(t) \end{bmatrix} + \begin{bmatrix} 0 \\ A \end{bmatrix} u(t) \\ z(t) &= \begin{bmatrix} 1 & 0 \end{bmatrix} \begin{bmatrix} p(t) \\ v(t) \end{bmatrix}. \end{aligned}$$

G. Sidebar: A Brief Historical Review of the Allan Variance

The Allan Variance (AV) was originally proposed in the 1960's for the study of frequency stability of oscillators and signal generators [49], [50], [87]. Since its definition, the AV has found utility for the specification of IMU performance. The IEEE standards are written in terms of the AV [28], [29], [30]. This section provides a very brief introduction to the history of the AV.

Consider a signal generator with instantaneous output voltage $V(t)$ given by,

$$V(t) = [V_0 + \epsilon(t)] \sin[2\pi\nu_0 t + \varphi(t)] \quad (92)$$

where V_0 and ν_0 are the nominal output amplitude and frequency, respectively; and $\epsilon(t)$ and $\varphi(t)$ are the instantaneous random amplitude and phase fluctuations. From $\varphi(t)$, the instantaneous fractional frequency fluctuation $u(t)$ is defined as,

$$u(t) = \frac{\dot{\varphi}(t)}{2\pi\nu_0}. \quad (93)$$

Before the introduction of the AV, the standard measure of frequency stability was the spectral density $S_u(f)$. The AV is an alternative, time-domain measure of frequency stability defined as

$$\sigma_u^2(\tau : N, T_s) = \left\langle \frac{1}{N-1} \sum_{k=1}^N \left(\bar{u}_k - \frac{1}{N} \sum_{j=1}^N \bar{u}_j \right)^2 \right\rangle. \quad (94)$$

The notation $\sigma_u^2(N, T_s, \tau)$ is standard in the AV literature. This Sidebar uses the more descriptive notation $\sigma_u^2(\tau : N, T_s)$ to indicate that N and T_s are parameters that the analyst selects to evaluate the value at cluster duration τ . In this notation, N is the number of clusters of duration τ that are used in the computation and T_s is the time between the start of consecutive clusters. The operator $\langle \cdot \rangle$ indicates an infinite time-average. In eqn. (94):

$$\bar{u}_k = \frac{1}{\tau} \int_{t_k}^{t_k+\tau} u(t) dt \quad (95)$$

with $t_k = t_{k-1} + T_s$. The expression in eqn. (94) can be understood as the sample variance of N averages of $u(t)$ each over a time interval of duration τ . The minimum value of τ and T_s is the sample period T . The symbols used in this discussion are defined in Table III. The relationship between these parameters is illustrated in Fig. 12. In the case where the time interval satisfies $T_s > \tau$, the computation has dead-time between clusters where data is unused.

The ‘‘Two-Sample Without Dead-Time’’ formula

$$\sigma_u^2(\tau) \equiv \langle \sigma_u^2(\tau : 2, \tau) \rangle = \left\langle \frac{(\bar{u}_{k+1} - \bar{u}_k)^2}{2} \right\rangle. \quad (96)$$

TABLE III
SYMBOLS USED IN THE DISCUSSION OF ALLAN VARIANCE.

Symbol	Meaning
T	Sample period for $u(t)$
L	Total number of samples in the data set
LT	Duration of the data set
τ	Cluster or averaging duration
n	Number of sample periods per cluster: $\tau = nT$
N	Number of clusters of duration τ used in eqn. (94)
m	Number of values of $\sigma_u^2(\tau : 2, \tau)$ averaged in eqn. (97)
t_k	Start time of the k -th averaging interval, see eqn. (95)
T_s	Time interval between consecutive averaging intervals
\bar{u}_k	Average of $u(t)$ for $t \in [t_k, t_k + \tau]$, see eqn. (95)

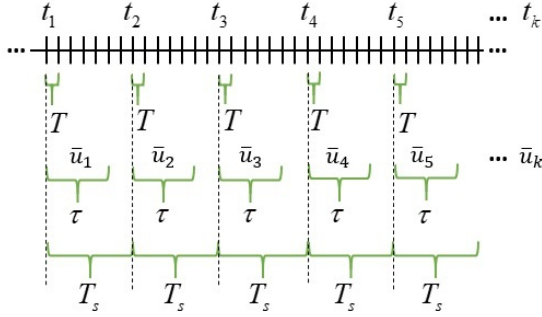


Fig. 12. Relationship between T , τ , T_s , t_k , and \bar{u}_k for this example: $\tau = 5T$ and $T_s = 7T$; therefore, it has a dead-time of $2T$.

(i.e., $\langle \sigma_u^2(N=2, T_s=\tau, \tau) \rangle$ in the standard notation) is recommended in [49], [50] and eventually became known as the “Allan Variance”.

Since practical data records are of finite length, the infinite time averages are not available; therefore, approximations are required. Barnes *et al.* [50] proposed and studied

$$\hat{\sigma}_u^2(\tau) = \frac{1}{2(m-1)} \sum_{k=1}^{m-1} (\bar{u}_{k+1} - \bar{u}_k)^2. \quad (97)$$

Note the hat in the left-side of eqn. (97) which indicates that it is designed as an estimate of $\sigma_u^2(\tau)$ defined in eqn. (96). This formula has become known as the “Non-Overlapping” AV, in reference to the fact that $T_s = \tau$.

Because the duration of the available data set is finite, for each value of τ and choice of T_s , the number of clusters m will change, with longer clusters and larger values of T_s yielding smaller values of m . Given a data record with L samples and a constant sample period T , the total experiment duration is LT seconds. The number of averages \bar{u}_k that can be computed (i.e., clusters) for a cluster duration of $\tau = nT$, without dead-time, is $m = L/n$.

Several alternative AV formulae have been proposed based on different choices for T_s . For instance, Howe, Allan and Barnes [88] introduced the (Fully) Overlapping AV with $T_s = T$ (which is the same as eqn. (12)):

$$\hat{\sigma}_u^2(\tau) = \frac{1}{2(L-2n)} \sum_{k=1}^{L-2n} (\bar{u}_{k+n} - \bar{u}_k)^2. \quad (98)$$

Its stated objective is to provide the best confidence in the estimates, which is achieved by high data utilization, i.e., the

TABLE IV
MAIN AV ESTIMATION FORMULAE

AV Estimate	Stated Benefits	Selected References
Non-Overlapping with Dead-Time (NODT)	—	[49], [38], [91], [92], [93], [94], [95]
Non-Overlapping (NO)	Simpler to compute (compared to NODT)	[50], [51], [52], [96], [92], [97]
Overlapping (O)	Gives high data utilization/better confidence in the estimate (compared to NO)	[88], [98], [99], [100]
Modified (M)	Able to better distinguish some types of noise (compared to O)	[87], [100], [101]
Not-Fully-Overlapping (NFO)	More computational efficient (compared to O)	[54]

number of formed averages \bar{u}_k is no longer $m = L/n$, but instead, $m = L - n$; therefore, the estimation accuracy of the Overlapping AV (based on $(L - 2n)$ differences) increases dramatically (relative to the Non-Overlapping AV) for long cluster-times. The Overlapping AV has since become the standard for IMU stochastic error modeling [28], [29].

Allan and Barnes [87] modified the Overlapping AV to improve its ability to distinguish stochastic processes with spectral densities $S_u(f) \approx f^\alpha$, such that $\alpha = +1$ or $+2$ (flicker phase noise, and white phase noise, respectively); however, these are generally not the main sources of stochastic errors corrupting an IMU (see eqn. (17)).

A more recent alternative to eqn. (98) is the Not-Fully-Overlapping AV, wherein $\tau > T_s > T$ [54]. In the article, the authors show that the method has similar estimation accuracy to the (Fully) Overlapping AV, but at a reduced computational cost, which is relevant because AV analysis for IMU characterization generally requires large datasets.

It is not the purpose of this tutorial to cover, in detail, the historical development of the AV [48], [89], [90]. For the interested reader, Table IV summarizes and compares various formulations of the AV and provides pointers to selected references.

H. Sidebar: Discussion of Eqn. (62)

Eqn. (62) appears to be counter-intuitive. Why would the discrete-time measurement variance Q_{η_d} decrease as the sample period T increases? This phenomenon has a long history that can be understood from different perspectives.

Sensor Model. The general assumption is that a discrete-time measurement is obtained as the mean of the continuous-time

quantity within the sample interval:

$$\tilde{u}(k) = \frac{1}{T} \int_{t_k}^{t_{k+1}} (u(\tau) + \eta_\omega(\tau)) d\tau \quad (99)$$

$$\tilde{u}(k) = \bar{u}(k) + \frac{1}{T} \int_{t_k}^{t_{k+1}} \eta_\omega(\tau) d\tau \quad (100)$$

$$\tilde{u}(k) = \bar{u}(k) + \eta(k), \quad (101)$$

where the discrete-time measurement noise is

$$\eta(k) = \frac{1}{T} \int_{t_k}^{t_{k+1}} \eta_\omega(\tau) d\tau. \quad (102)$$

If $\eta_\omega(\tau)$ is white, then its covariance function is $E\langle\eta_\omega(\zeta)\eta_\omega(\tau)\rangle = S_N \delta(\zeta - \tau)$ where δ denotes the Dirac delta function and S_N is the PSD. Therefore, the covariance of $\eta(k)$ is computed as

$$\begin{aligned} Q_{\eta_d}(k) &= E\langle\eta(k)\eta(k)\rangle \\ &= E\left\langle\left(\frac{1}{T} \int_{t_k}^{t_{k+1}} \eta_\omega(\tau) d\tau\right)\left(\frac{1}{T} \int_{t_k}^{t_{k+1}} \eta_\omega(\zeta) d\zeta\right)\right\rangle \\ &= \frac{1}{T^2} \int_{t_k}^{t_{k+1}} \int_{t_k}^{t_{k+1}} E\langle\eta_\omega(\tau)\eta_\omega(\zeta)\rangle d\zeta d\tau \\ &= \frac{1}{T^2} \int_{t_k}^{t_{k+1}} \int_{t_k}^{t_{k+1}} S_N \delta(\zeta - \tau) d\zeta d\tau \\ &= \frac{1}{T^2} \int_{t_k}^{t_{k+1}} S_N d\tau \\ Q_{\eta_d}(k) &= \frac{1}{T} S_N \end{aligned} \quad (103)$$

which is the same as eqn. (62).

Angle Increments. From eqn. (99), the discrete-time IMU samples may be presented (i.e., scaled) as either an angular rate (or acceleration) measurement $u(k)$ or an angle (or velocity) increment $\Delta(k) = u(k)T$ over the time increment of length T . The analysis of eqns. (56-62) presented the IMU white noise conversion from continuous to discrete time for the first case: IMU angular rate (or acceleration) outputs, which resulted in eqn. (62). This section considers the analysis for the case where IMU outputs angle (or velocity) increments.

The discrete-time model that is equivalent to eqn. (51) is

$$x_v(k+1) = x_v(k) + \Delta(k). \quad (104)$$

The discrete-time model that is equivalent to eqn. (52) is

$$\hat{x}_v(k+1) = \hat{x}_v(k) + \tilde{\Delta}(k). \quad (105)$$

Scaling both sides of eqn. (58) by T yields the discrete-time measurement model,

$$\tilde{\Delta}(k) = \Delta(k) + \eta_\Delta(k), \quad (106)$$

with white measurement noise $\eta_\Delta(k) \sim N(0, Q_{\eta_\Delta})$. By the definition of $\Delta(k)$ in the previous paragraph, $Q_{\eta_\Delta} = T^2 Q_{\eta_d}$, where Q_{η_d} is defined in eqn. (45). The error signal $e(k) = x_v(k) - \hat{x}_v(k)$ has the time propagation model

$$e(k+1) = e(k) - \eta_\Delta(k) \quad (107)$$

which is a discrete-time random walk process. The discrete-time propagation of the covariance of $e(k)$ driven by $\eta_\Delta(k)$ is

$$P_e(k+1) = P_e(k) + Q_{\eta_\Delta} \text{ for any } k \geq 0. \quad (108)$$

Due to the assumption that the initial covariance of $e(k)$ is zero, eqn. (108) simplifies to

$$P_e(k) = k Q_{\eta_\Delta}. \quad (109)$$

Because the continuous and discrete time models are equivalent, their covariance must be the same at the discrete sample times. Equating eqn. (55) to eqn. (109), yields:

$$\begin{aligned} P_e(t)|_{t=kT} &= P_e(k) \\ S_N k T &= k Q_{\eta_\Delta}, \end{aligned}$$

which provides the equation,

$$Q_{\eta_\Delta} = S_N T \quad (110)$$

which is equivalent to eqn. (62) because $Q_{\eta_\Delta} = T^2 Q_{\eta_d}$.

The fact that the PSD S_N must be equal to $\frac{Q_{\eta_\Delta}}{T}$ is discussed in Example 3.20 in [102] which attributes that example to Kalman in [103]. The example discusses continuous-time white noise as the limit of discrete-time white noise as T approaches zero.

Unit Analysis. Consider the units of S_N , Q_{η_Δ} , and Q_{η_d} .

- The symbol S_N represents the power spectral density of $\eta_z(t)$, which has units of $\frac{(deg/s)^2}{Hz} = \frac{(deg)^2}{s}$ for gyros and $\frac{(m/s^2)^2}{Hz} = \frac{(m)^2}{s^3}$ for accelerometers.
- The symbol Q_{η_d} represents the covariance of $\eta(k)$, which has units of $(deg/s)^2$ for gyros and $(m/s^2)^2$ for accelerometers.
- The symbol Q_{η_Δ} represents the covariance of $\eta_\Delta(k)$, which has units of $(deg)^2$ for gyros and $(m/s)^2$ for accelerometers.

Note that all these units work out consistently in eqns. (62) and (110). Eqn. (62) is used to compute the covariance of the discrete-time white noise covariance Q_{η_d} , which is needed for the design of the state estimator, from the continuous-time PSD S_N , which is extracted from the ASD.

XI. SHORT BIOGRAPHY FOR EACH AUTHOR

A. Farrell

Jay A. Farrell received B.S. degrees in physics and electrical engineering from Iowa State University, and M.S. and Ph.D. degrees in electrical engineering from the University of Notre Dame. At Charles Stark Draper Lab (1989-1994), he was principal investigator on projects involving autonomous vehicles, receiving the Engineering Vice President's Best Technical Publication Award in 1990, and Recognition Awards for Outstanding Performance and Achievement in 1991 and 1993. He is the KA Endowed Professor in the Department of Electrical and Computer Engineering at the University of California, Riverside. For the IEEE Control Systems Society (CSS), he has served as Vice President Finance, Vice President of Technical Activities, CSS General Vice Chair of IEEE CDC-ECC 2011, General Chair of IEEE CDC 2012, President Elect, President, and Past President. For IEEE he served three terms on the Fellow Committee, as EAB Treasurer, and on IEEE FinComm. He is currently President of AACC. He is author of over 250 technical articles and three books. He was recognized as a GNSS Leader to Watch by GPS World Magazine in 2009 and is a Distinguished Member of IEEE CSS, a Fellow of the IEEE, a Fellow of AAAS, and a Fellow of IFAC.

B. Silva

Felipe O. Silva received the B.S. Degree in Automatic Control Engineering (with honors) from the Federal University of Itajubá, in Brazil (2012); the M.S. degree in Systems Engineering from the National Institute of Applied Sciences, Center Val de Loire, in France (2013); and the Ph.D. Degree in Aeronautical and Mechanical Engineering from the Aeronautics Institute of Technology, in Brazil (2016). From 2013 to 2014, he was an Assistant Researcher with the Institute of Aeronautics and Space, in Brazil. Since 2014, he has been an Assistant Professor with the Federal University of Lavras, in Brazil. Since 2017, he has been an Associate with the technology-based microenterprise Inovação em Mecanização Agrícola Ceifa Ltda., in Brazil. In 2018, he was a Visiting Professor with the Central School of Nantes, in France. From 2018 to 2019, he was a Visiting Professor with the University of California Riverside, in Riverside, USA. His research area includes: Guidance, Navigation and Control Systems; Inertial Navigation Systems; Global Navigation Satellite Systems; Sensor Fusion; Instrumentation; Robotics; Hydro-Pneumatic Systems and Precision Agriculture. Since 2020, he has been a member of the Brazilian Computer Society.

C. Rahman

Farzana Rahman received the Ph.D. degree in Electrical and Computer Engineering from University of California, Riverside, in 2020 and the B.S. degree in Electrical Engineering from Bangladesh University of Engineering and Technology, in 2014. She currently works as a Software Engineer at Nuro, working on robotics and self-driving vehicles. Her current research interests include robot localization and mapping algorithm design.

D. Wendel

Jan Wendel received the Dipl.-Ing. and Dr.-Ing. degrees in Electrical Engineering from the University of Karlsruhe, Germany, in 1998 and 2003, respectively. From 2003 until 2006 he was an assistant professor at the University of Karlsruhe, where he was private lecturer until 2018. In 2006, he joined MBDA in Munich, Germany, working on the development of navigation algorithms for various applications. In 2009, he joined Airbus Defense and Space in Munich, where he is involved in various activities related to satellite navigation including acquisition and tracking algorithms, interference detection and characterization, integrity algorithms, and PRS receiver development.